Validation of a tearing mode locking model using a database of disruptive plasmas at ASDEX Upgrade

V. Klevarová[1], H. Zohm[2], G. Pautasso[2], G. Tardini[2], R. McDermott[2],
G. Verdoolaege[1,3], J. Snipes[4], P.C. de Vries[4], M. Lehnen[4], the EUROfusion MST1
team[†], and the ASDEX Upgrade team[⋆]

[1]Department of Applied Physics, Ghent University, Sint-Pietersnieuwstraat 41, 9000
Ghent, Belgium, [2]Max-Planck-Institut für Plasmaphysik, 85748 Garching, Germany,
[3]Laboratory for Plasma Physics, Royal Military Academy (LPP-ERM/KMS), 1000
Brussels, Belgium, [4]ITER organization, Route de Vinon sur Verdon, CS 90 046,
13067, St. Paul-lez-Durance, France, [†]See the author list of H. Meyer et al. 2019 Nucl.
Fusion 59 112014, [⋆]See the author list of B. Labit et al. 2019 Nucl. Fusion 59 0860020

Abstract

An exploratory study is presented that aims at validating a model for mode locking on
the basis of a large set of ASDEX Upgrade (AUG) discharges. Not discriminating between
plasma configurations, the model allows to estimate the duration of the deceleration
phase, as well as the critical mode width for locking. Both quantities are important for
the design of disruption avoidance algorithms that aim to affect the MHD mode rotation.
It was found that the model successfully described locking of large modes in those cases
where the deceleration started in a quasi-stationary phase of the discharge (i.e. with low
variability of the global plasma angular momentum prior to mode seeding) and where
deceleration took place over temporal intervals comparable to the momentum confinement
time. Theoretical braking curves and locking durations predicted with the model were in
good quantitative agreement with the experiment. On the other hand, the model failed
to reproduce the braking curves of modes appearing towards the end of a transient phase,
e.g. during an impurity influx or when approaching the disruptive density limit. It can
be concluded that the modes were not the primary cause of the plasma momentum losses
within the scope of the model. A modified mode equation of motion is proposed, which
accounts for transient variation of the plasma density, e.g. during the development of a
MARFE, and its impact on braking predictions is discussed. Furthermore, it was observed
that a substantial fraction of modes was rotating at the onset of a major disruptive event.
Consequences of this observation on disruption prediction schemes in AUG are examined.

1 Introduction

Tokamak disruptions, fast losses of the plasma confinement, represent a potential threat to
future large devices in terms of heat and particle loads on the plasma-facing materials and
electromagnetic forces applied on the in-vessel components [1]. Analysis of a large number
of disruptions in JET revealed that a primary cause of the major thermal quench (sudden
drop in the plasma energy content) was a tearing mode [2] of critical amplitude [3], static
in the laboratory frame—the so-called *locked mode*. The amplitude of the tearing instability
thus represents an important quantity to consider in physics-driven (i.e. based on physi-
cal models and scalings) disruption prediction schemes. Prior to locking, modes are often
observed to rotate. Given the stabilizing effect of conducting structures on rotating modes
(supported by differential rotation of the resonant surfaces), maintaining (or increasing) the
mode rotation frequency is a key instrument for disruption avoidance [4–7]. Losses of the
mode angular momentum leading to locking appear to be linked to the width of the instabil-
ity [8,9]. Efforts to reduce the radial extent of the mode in real time have involved current

drive and heating localized on the rational surface of interest [10–12]. A combination of sustained plasma rotation and reduction of the mode width could therefore be instrumental for disruption avoidance schemes, thus maintaining good plasma confinement, and directing the discharge parameters towards a non-disruptive area of the device operational space. Hence, the expected *duration of the locking phase* is a key information that should be provided to the plasma control system for disruption avoidance, in order to determine the settings of the actuators affecting the mode rotation frequency and instability width. In addition, the *critical island width for locking* can serve as a warning to prepare the plasma control system for a potentially disruptive state. Both quantities should be accessible in real time during the discharge.

In this paper, we intend to demonstrate that the locking phase duration and critical island width may be obtained in real time on the basis of a physical model for mode braking. Variants of the model used in this paper have been formulated in the past [13–15] and have yielded useful input for the design of disruption avoidance actuators [14, 16]. Unlike future fusion power plants, present experimental tokamak devices operate over a broad range of plasma conditions. The plasma state is often close to certain operational limits, where rotating MHD modes can be driven unstable, which may later disrupt the plasma. It is thus of interest to validate the mode locking model for a large set of discharges, thereby considering a broad variety of operational scenarios, plasma parameters, discharge phases, as well as root causes for mode initiation and details of the mode growth. This allows to explore the limitations of the model and may provide guidelines for its improvement. For this purpose, a large database of disruptive discharges was assembled in ASDEX Upgrade (AUG) with initially rotating tearing modes. The database contains a broad variety of braking dynamics, ranging from fast growing and locking modes to quasi-stable islands braking over long temporal periods. The physical braking model was invoked with the aim to reproduce the experimental braking curves, accounting for multiple scenarios of momentum transfer at the interface between the mode and the bulk plasma, in order to identify the scenario that best explains the experimental observations. In addition, key predictions by the model (braking phase duration and critical mode width for locking) were compared with the experiment and, in the event of a discrepancy, the possible causes were examined.

The contents of the paper are as follows. In Sec. 2, the physical model for mode deceleration is presented. The dynamic critical condition for locking, accounting for the mode growth and momentum redistribution rate, is derived. Sec. 3 presents the database of disruptive plasmas, including classification of disruption types, and discusses validation of the experimental input necessary for application of the braking model. In Sec. 4, a critical condition for locking is evaluated both theoretically and experimentally for selected cases. Reconstruction of braking curves is presented and situations where the model breaks down are investigated in detail. The role of rotating modes in the disruption onset is studied in Sec. 5. Sec. 6 contains a discussion of the results, as well as model limitations and potential extensions, and Sec. 7 concludes the paper.

2 Tearing mode braking model

2.1 Mode dynamics

The rotation of tearing modes is assumed to be composed of the toroidal motion of the plasma bulk ions and the electron diamagnetic drift [17, 18]. The rate of change of the mode angular frequency ω may be expressed as a sum of forces acting on the mode. We assume that the rotation is driven by viscous coupling between the mode and the bulk plasma and mode deceleration via electromagnetic interaction with the wall of finite resistivity [14]:

$$\frac{\mathrm{d}\omega}{\mathrm{d}t} = F_{\mathrm{VS}} - F_{\mathrm{RW}}. \tag{1}$$

Here, the respective force terms (encompassing the moment of inertia associated with the braking mass) are denoted by F_{VS} and F_{RW}. The interaction with the device error fields is neglected, since the intensity of error fields is assumed to be small in AUG, becoming important only at the final stage of locking [19]. The plasma poloidal rotation is assumed to be damped [20], so the following discussion will only concern the forces affecting the motion in the toroidal direction.

The model for the viscous force term F_{VS} states that any deviation of the mode rotational frequency from the stationary state ω_0, is counteracted by the perpendicular viscous plasma-mode coupling [18]. The restoring viscous torque is proportional to $\omega - \omega_0$, with the proportionality factor containing the momentum diffusivity coefficient. Specifically, we adopt the following expression for the viscous restoring force [14]:

$$F_{VS} = \frac{\omega_0}{\tau_{M0}} - \frac{\omega}{\tau_M}. \tag{2}$$

Herein, the global momentum confinement time τ_M is related to the plasma viscosity, where

$$\tau_M = L_\phi / T_{IN} = \frac{1}{T_{IN}} \int m_{eff} n_e R^2 \omega \, dV, \tag{3}$$

with L_ϕ the total toroidal angular momentum, T_{IN} the total torque input and m_{eff} the effective nucleon number. In NBI-heated discharges, T_{IN} may be fully determined by the torque induced by the beams, i.e. $T_{IN} \approx T_{NBI}$. It should be noted that macroscopic MHD modes are known to deteriorate global confinement properties. In [9], a model describing this deterioration was developed, resulting in an expression for a decrement $\Delta\tau_{E,dec}$ of the energy confinement time, following the growth of the instability. It was shown that $\Delta\tau_{E,dec}$ depends on the normalized radius of the mode's rational surface r_s/a (a is the plasma minor radius), as well as the island width w. Often, one can approximate τ_M by τ_E, with some exceptions, e.g. in the case of discharges with peaked density profiles [21]. Therefore, following [14], we take the momentum confinement deterioration by the mode into account by including in the mode locking model a correction of τ_M:

$$\tau_M = \frac{\tau_{M0}}{1 + f_M w/a}. \tag{4}$$

Here, the subscript '0' refers to the mode-free phase of the discharge and f_M is a constant factor that is assumed to represent various effects of confinement degradation not specified in any further detail. Experimentally, it is difficult to isolate from f_M the effect on the confinement of the mode braking due to the wall drag. Other phenomena, such as the H-to-L transition, which usually precedes the disruption onset, contribute to the confinement deterioration as well.

The resistive wall force term was introduced in [13] and its analytical expression for a mode with poloidal mode number m is the following:

$$F_{RW} = -A \frac{\omega\tau_w}{(\omega\tau_w)^2 + m^2} \left(\frac{w}{a}\right)^4. \tag{5}$$

Here, τ_w is the resistive wall time, given by

$$\tau_w = \frac{\mu_0 \sigma_w b r_w}{2}, \tag{6}$$

where b is the wall thickness, σ_w its conductivity and r_w is the minor radius of the wall. In addition, A is a parameter depending on the mass subjected to braking, where two scenarios of momentum transfer can be considered at the interface between the mode and the plasma bulk:

- Mode momentum losses are perfectly coupled to the motion of the plasma bulk, implying common deceleration. This scenario will be indicated by the subscript 'co'.

- The island deceleration is completely decoupled from the plasma, indicated by the subscript 'de'.

Both situations are illustrated in Fig. 1. In the case of perfect coupling, the radial momentum transfer is maximised and the local momentum losses experienced by the mode are instantaneously transferred to deceleration of the plasma bulk over the full radial extent. On the other hand, in the decoupled case the momentum diffusivity at the radii $r_\mathrm{s} \pm w/2 = 0$ is zero. In JET, it has been reported that the experimental situation is likely a compromise between the two variants [22]. In this paper, we mainly consider the 'no-slip' condition, i.e. the 'co' scenario with equal rotation frequency of island and plasma bulk, theoretically applying to large-amplitude modes [23]. For the parameter A we obtain the following analytical expressions for the 'co' and 'de' scenarios, respectively, assuming a flat density profile [13]:

$$A_\mathrm{co} = \left(\frac{m}{16}\right)^2 \left(\frac{r_\mathrm{s}}{r_\mathrm{w}}\right)^{2m} \left(\frac{q'}{q}\right)^2_{r_\mathrm{s}} \frac{a^2 B_\theta^2(r_\mathrm{s})}{\mu_0 n_\mathrm{e} m_\mathrm{i}} \frac{2n^2}{R_0^2} = \frac{A_0}{\tau_\mathrm{A,co}^2}, \tag{7}$$

$$A_\mathrm{de} = \left(\frac{m}{16}\right)^2 \left(\frac{r_\mathrm{s}}{r_\mathrm{w}}\right)^{2m} \left(\frac{q'}{q}\right)^2_{r_\mathrm{s}} \frac{a^2 B_\theta^2(r_\mathrm{s})}{\mu_0 n_\mathrm{e} m_\mathrm{i}} \frac{a^2}{r_\mathrm{s} w} \frac{n^2}{R_0^2} = \frac{A_0}{\tau_\mathrm{A,de}^2}. \tag{8}$$

Here, q is the safety factor, q' its radial derivative, n the toroidal mode number, R_0 the tokamak major radius,

$$A_0 = \frac{m^2}{256} \left(\frac{r_\mathrm{s}}{r_\mathrm{w}}\right)^{2m} \left(\frac{q'}{q}\right)^2_{r_\mathrm{s}} a^2$$

and

$$\tau_\mathrm{A,co}^2 = \frac{\mu_0 n_\mathrm{e} m_i R_0^2}{2n^2 B_\theta^2(r_\mathrm{s})}, \qquad \tau_\mathrm{A,de}^2 = \frac{\mu_0 n_\mathrm{e} m_i R_0^2 r_\mathrm{s} w}{n^2 B_\theta^2(r_\mathrm{s}) a^2} \quad (n_\mathrm{e} \approx n_\mathrm{i})$$

are the associated Alfvén times.

The locking duration t_lock, one of the parameters of interest within the scope of disruption avoidance, is defined as the time interval from the initiation of the frequency decay from the mode's initial angular frequency ω_0 until the locked state. It can be shown that for a mode growth prescribed by a power law in η

$$\frac{w}{a}(t) = (\gamma t)^\eta + \left(\frac{w}{a}\right)_\mathrm{off}, \tag{9}$$

with γ a parameter describing the mode growth rate, $(w/a)_\mathrm{off}$ an offset mode width and under the condition $\omega_0 \tau_\mathrm{w}/\sqrt{2} \gg m$, the ratio of the braking phase durations for the 'co' and 'de' scenarios is the following:

$$\frac{t_\mathrm{lock,co}}{t_\mathrm{lock,de}} = \left(\frac{A_\mathrm{de}}{A_\mathrm{co}}\right)^{1/5} = \left(\frac{1}{2}\frac{a^2}{r_\mathrm{s} w}\right)^{1/5}. \tag{10}$$

This implies that $t_\mathrm{lock,co} > t_\mathrm{lock,de}$.

Finally, combining (1) with (2) and (5) yields the expression for the frequency evolution of the mode:

$$\frac{d\omega}{dt} = \frac{\omega_0}{\tau_\mathrm{M0}} - \frac{\omega(1 + f_\mathrm{M} w/a)}{\tau_\mathrm{M0}} - A\left[\frac{w}{a}(t)\right]^4 \frac{\omega \tau_\mathrm{w}}{(\omega \tau_\mathrm{w})^2 + m^2}. \tag{11}$$

Numerical integration of (11) was used to reconstruct braking curves, i.e. plots of the mode rotational frequency $\omega_\mathrm{int}(t)$ as a function of time ('int' stands for 'integrated'). This also provides an estimate of the braking duration t_lock. The critical condition for locking is discussed in Secs. 2.2 and 2.3 below.
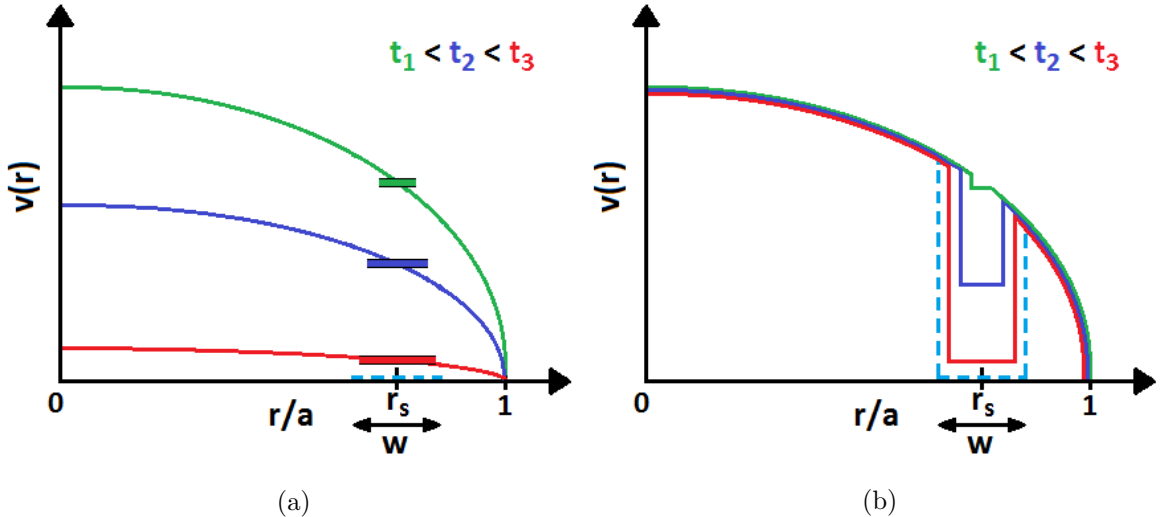
Figure 1: Schematic illustration of the rotational velocity profile $v(r)$ for the two extreme scenarios 'co' and 'de' for mode deceleration. The profile is depicted at three time points for an island of progressively increasing width w, located at a rational surface of radius $r = r_s$. Panel (a) displays the situation in which momentum losses experienced by the mode are transferred instantaneously to the plasma bulk braking (case 'co'). In (b), the island deceleration is fully decoupled from the plasma bulk movement (case 'de').

τ_w (ms)	q_{95}	R_0 (m)	$\omega_0/2\pi$ (kHz)	τ_{M0} (ms)	m/n
1.0	3.6	1.65	3.5	50	2/1

f_M	I_p (MA)	B_t (T)	n_e (m^{-3})	r_w/a	ν
0	1.0	2.5	5.0×10^{19}	1	2

Table 1: Parameter values used for obtaining the solutions of the mode equation of motion shown in Fig. 2.

2.2 Condition for mode locking

For the purpose of derivation of the condition for mode locking, we will first examine stationary solutions of (11). Those represent, for a given mode width, situations with balanced forces [15, 24]. Solving the rotational frequency from the force balance for a scan of island widths a stationary braking curve can be obtained. An example for the case of the 'co' scenario, also indicating the island width prescribed by (9), is shown in Fig. 2a ($1/\gamma = 50$ ms, $(w/a)_{\text{off}}$, $f_M = 0$, other parameters are given in Tab. 1). Using the figure, it is possible to easily extract the solution of balanced forces in the frequency domain by intersecting the braking curve with a vertical line placed at the examined island width.

For a certain range of w/a, restricted by red and black arrows in Fig. 2, multiple solutions of the force balance exist and the braking curve will be intersected two or three times. In addition, it turns out that the stationary solutions are real if the following condition is met (cyan arrow):

$$A\tau_M\tau_w \left(\frac{w}{a}\right)^4 > 8m^2. \tag{12}$$

This condition can be derived upon calculation of solutions of the time-independent form of (11), reformulated in terms of dimensionless $\omega\tau_w$. This leads to the following cubic equation:
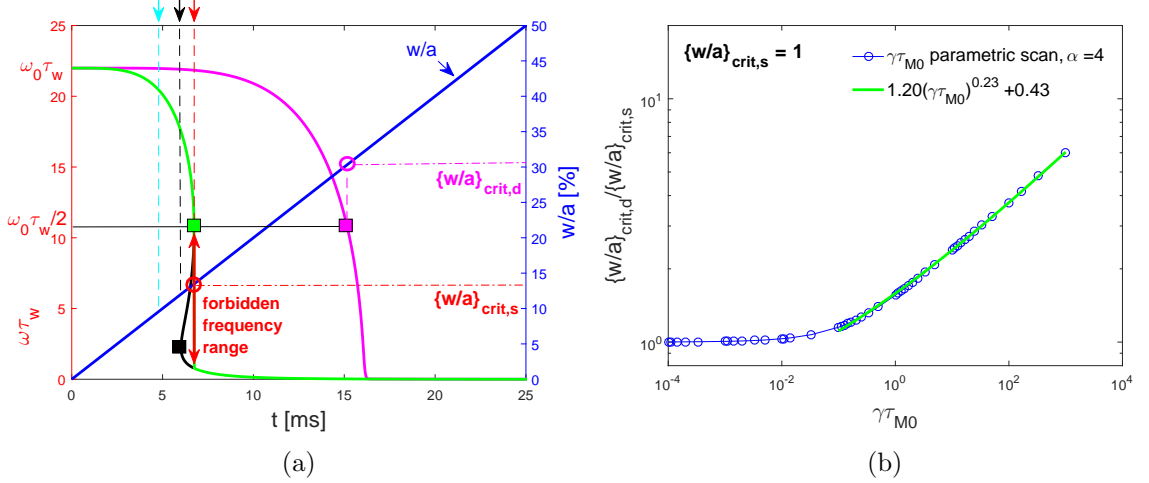
Figure 2: (a) Comparison of stationary (green and black) and dynamic (magenta) braking curves in the 'co' scenario. The cyan arrow refers to condition fulfilment of (12). For any increasing w/a, the solutions of (13) are real. The black and red arrows delimit the interval of w/a for which multiple force balance solutions exist. The range of 'forbidden' frequencies is depicted by the double red arrow. (b) The blue solid line indicates $(w/a)_{\mathrm{crit,d}}/(w/a)_{\mathrm{crit,s}}$ for a parametric scan of $\tilde{\gamma} = \gamma \tau_{\mathrm{M0}}$ in the 'co' scenario, with $\alpha = 4$ (the individual points of the scan are encircled). The bold green line results from a fit of the function $(w/a)_{\mathrm{crit,d}}/(w/a)_{\mathrm{crit,s}} = c_1(\gamma \tau_{\mathrm{M0}})^{c_2} + c_3$ to the scan points (restricted to $\tilde{\gamma} \gtrsim 0.1$).

$$(\omega \tau_{\mathrm{w}})^3 - (\omega \tau_{\mathrm{w}})^2 \frac{\omega_0 \tau_{\mathrm{w}}}{1 + f_{\mathrm{M}} w/a} + \omega \tau_{\mathrm{w}} \left[m^2 + A \tau_{\mathrm{M0}} \tau_{\mathrm{w}} \left(\frac{w}{a} \right)^4 \frac{1}{1 + f_{\mathrm{M}} w/a} \right] - \frac{\omega_0 \tau_{\mathrm{w}} m^2}{1 + f_{\mathrm{M}} w/a} = 0. \quad (13)$$

A locking bifurcation occurs at a critical island width $(w/a)_{\mathrm{crit,s}}$ (the subscript 's' refers to the condition of stationarity). At this mode width, an unstable solution of the force balance is met. Fluctuations in the frequency domain around this point lead to adopting the root of (13) at the lower end of the so called forbidden frequency band. The point of bifurcation defines the critical condition for mode locking.

For an increasing island width, the condition given by (12) is amplified, i.e. $A \tau_{\mathrm{M}} \tau_{\mathrm{w}} (w/a)^4 \gg 8m^2$. Under this condition it is possible to adopt a high-frequency limit of (13), simplifying it to a quadratic function. The point of locking bifurcation can then be analytically expressed as:

$$\left(\frac{w}{a} \right)^2 \left[\left(1 + f_{\mathrm{M}} \frac{w}{a} \right)^{3/2} + \left(1 + f_{\mathrm{M}} \frac{w}{a} \right)^{1/2} \right] = \frac{\omega_0 \tau_{\mathrm{w}}}{\sqrt{A \tau_{\mathrm{M0}} \tau_{\mathrm{w}}}}. \quad (14)$$

Further simplification is possible by assuming that the momentum confinement is not affected by the mode ($f_{\mathrm{M}} = 0$ in (4)). For the coupled and decoupled situations, this yields

$$(w/a)_{\mathrm{crit,s,co}} = \left(\frac{\omega_0 \tau_{\mathrm{A,co}}}{2} \right)^{1/2} \left(\frac{\tau_{\mathrm{w}}}{\tau_{\mathrm{M0}} A_0} \right)^{1/4}, \quad (15)$$

$$(w/a)_{\mathrm{crit,s,de}} = \left(\frac{\omega_0 \tau_{\mathrm{A,de}} a}{2w} \right)^{2/3} \left(\frac{\tau_{\mathrm{w}}}{\tau_{\mathrm{M0}} A_0} \right)^{1/3}, \quad (16)$$

Recall that $\tau_{\mathrm{A,de}} \propto w/a$, therefore the right-hand side of (16) is independent of the island width. In [14], it has been shown that the locking bifurcation occurs at a mode frequency

$$(\omega \tau_{\mathrm{w}})_{\mathrm{crit}} = \frac{\omega_0 \tau_{\mathrm{w}}}{2(1 + f_{\mathrm{M}} w/a)}. \quad (17)$$

6

A single stationary solution of (11) for an arbitrary w/a is found if the following condition is satisfied [15]:

$$\omega_0 \tau_{\mathrm{w}} < 3\sqrt{3}m. \tag{18}$$

In that case, the point of locking bifurcation is not defined and the mode's rotational frequency decays as a continuous function (recall that the existence of a forbidden frequency range represents a discontinuity in the braking curve).

2.3 Static vs. dynamic critical island width

The condition for a locking bifurcation was derived assuming constant parameters appearing in the island equation of motion (11). In practice, such conditions can be reproduced when the mode width evolves on a time scale much longer than that of the momentum redistribution, determined by τ_{M}. In such cases, the braking and restoring forces applied on the decelerating mass balance each other at all times [25]. If the island width increases quickly relative to the momentum redistribution, the stationary critical island width $(w/a)_{\mathrm{crit,s}}$ is not an actual point of the locking bifurcation. According to (17), a locking bifurcation occurs at half of the initial rotational frequency of the mode ($f_{\mathrm{M}} \to 0$). In the remainder of this work, we *define* the critical island width $(w/a)_{\mathrm{crit,d}}$ on the time-dependent braking curve at the point where the bifurcation occurs (the subscript 'd' refers to 'dynamic'). An example of a dynamically integrated braking curve is shown in Fig. 2a (solid magenta line), with $\gamma\tau_{\mathrm{M0}} = 1$.

It is instructive to compare the stationary and dynamic critical island widths, defined above. Using (15) ('co') or (16) ('de') with the values in Tab. 1, $(w/a)_{\mathrm{crit,s}}$ can be calculated, where we assumed a current profile of the form $j(r) = j(0)[1 - (r/a)^2]^\nu$, with $j(0) = I_{\mathrm{p}}(\nu + 1)/\pi a^2$ and I_{p} the plasma current [26]. To calculate the dynamic $(w/a)_{\mathrm{crit,d}}$, (11) with $f_{\mathrm{M}} = 0$ was reformulated in terms of the ratio $w/a(t)/(w/a)_{\mathrm{crit,s}}$ and dimensionless variables $\tilde{t} = t/\tau_{\mathrm{M0}}$, $\tilde{\omega} = \omega/\omega_0$, $\tilde{\gamma} = \gamma\tau_{\mathrm{M0}}$. Using the expression for the mode width growth (9) ($\eta \geq 1$, $(w/a)_{\mathrm{off}} = 0$), this results in:

$$\frac{d\tilde{\omega}}{d\tilde{t}} = 1 - \tilde{\omega} - \frac{1}{4\tilde{\omega}}\left[\frac{\tilde{\gamma}\tilde{t}}{(w/a)_{\mathrm{crit,s}}}\right]^\alpha. \tag{19}$$

Here, $\alpha = 4\eta$ (i.e. $\alpha \geq 4$) for the 'co' case, while $\alpha = 3\eta$ ($\alpha \geq 3$) for 'de'. In addition, the high-frequency limit was adopted, assuming that $m \ll \omega_0\tau_{\mathrm{w}}$. Next, (19) was integrated until $t = 1$ s in the scope of a parametric scan, where $\tilde{\gamma}$ was varied over several orders of magnitude, keeping $\tau_M = \tau_{\mathrm{M0}}$ constant. Several values of α were tested during the scan. Furthermore, $(w/a)_{\mathrm{crit,s}}$ was set to a constant value to allow scan in $\tilde{\gamma}$, in particular to 1, since for this value the fit (described below) was of high confidence for the largest range of α. An example of a parametric scan in the 'co' scenario with $\alpha = 4$ is shown in Fig. 2b. For $\tilde{\gamma} \ll 1$, $(w/a)_{\mathrm{crit,d}}$ approaches $(w/a)_{\mathrm{crit,s}}$, since in this case the mode grows slowly in comparison with the momentum redistribution time scale. In the other limit it can be seen that $(w/a)_{\mathrm{crit,d}} \gg (w/a)_{\mathrm{crit,s}}$, suggesting that the mode grows too fast for the forces to balance.

Considering a reasonable range of machine sizes and plasma temperatures (determining the plasma resistivity, which in turn sets the actual mode growth rate), the lower limit of $\tilde{\gamma}$ can be estimated to lie around 0.1. Data resulting from the scan, restricted to this lower limit, were fitted with an analytical expression of the form $(w/a)_{\mathrm{crit,d}}/(w/a)_{\mathrm{crit,s}} = c_1[\gamma\tau_{\mathrm{M0}}/(w/a)_{\mathrm{crit,s}}]^{c_2} + c_3$. In turn, this was done for values of α within interval $\alpha = [3\ 10]$, and the curves $c_i(\alpha)$ ($i = 1, 2, 3$) were then fitted by a simple analytical function. This resulted in $c_1 \sim -0.035\alpha + 1.28$, $c_2 \sim 1/\alpha$ and $c_3 \sim 0.004\alpha + 0.26$. For a given set of input parameters, the expression for the critical island width for the 'co' scenario can be thus

formulated in the form ('fit' stands for 'fitted'):

$$\frac{(w/a)_{\text{crit,d,fit}}}{(w/a)_{\text{crit,s}}} = (-0.035\alpha + 1.28) \left[\frac{\gamma \tau_{\text{M0}}}{(w/a)_{\text{crit,s}}} \right]^{1/\alpha} + 0.004\alpha + 0.26. \qquad (20)$$

The variable $(w/a)_{\text{crit,s}}$ appears in (20) although strictly speaking, it was kept constant during the parametric scan. We test its generalization on the case of the example shown in Fig. 2a. There, $(w/a)_{\text{crit,s}} = 13.5\%$ (equation (15)), while $(w/a)_{\text{crit,d}} \approx 31.0\%$, i.e. more than two times larger. Equation 20 results in $(w/a)_{\text{crit,d,fit}} \approx 29.1\%$ which is a good approximation of $(w/a)_{\text{crit,d}}$. Hence, (20) will be used in the application of the mode locking model in Sec. 4 to evaluate the condition for the locking bifurcation. It should not be used, however, far outside the parameter space in which it was fitted. Equation (20) is suitable for a real-time evaluation of the condition for mode locking, but an information concerning the mode growth has to be submitted to the calculation. Finally, note that for $\tilde{\gamma} \gg 1$ the dynamic braking curves are always continuous functions (unlike in the stationary case due to existence of the forbidden frequency range), whether the condition (18) for the locking bifurcation is satisfied or not.

3   Database for validation of the mode locking model

3.1   Assembly of disruptive discharge database

Disruptive plasmas were identified among the discharges performed in AUG during the years 2012–2016, in the presence of the full tungsten wall. In this paper, a disruption is defined as a sudden drop in the plasma thermal energy content, followed by vertical destabilization of the plasma column. The database was populated with disruptions having a tearing mode as the final disruption precursor. In each case, the disruption time was set at the onset of the current spike with the largest amplitude, preceding the current quench. Furthermore, the discharges had to fulfil the following criteria to be included in the database:

- Vertically stable plasma column until the onset of the major disruption.

- Thermal quench not induced by a massive gas injection.

- No resonant magnetic perturbations coils in operation over the lifetime of the mode.

This resulted in a database consisting of 454 discharges.

Next, the database entries were grouped according to the main characteristics of the rotation dynamics:

- Modes rotating until the onset of the major disruption (ROT),

- Initially rotating instabilities decaying in frequency until becoming locked (ROT→LM),

- Born-locked modes (BLM).

The percentage fraction per group can be found in Tab. 2. Groups ROT and ROT→LM are of primary interest in the study presented here, as they are populated by initially rotating modes. To be eligible for further analysis, the input torque from the NBI heating modules had to remain constant during the locking (braking) phase. The reduced database of initially rotating disruptive modes fulfilling this additional criterion consists of more than 220 entries.

Full database	ROT	ROT→LM	BLM
454 entries	27%	54%	19%

Table 2: Total number of database entries and relative occurrence of mode groups within the full database of AUG disruptive discharges presented in this paper.

3.2 Disruption classification

The 454 discharges in the full database were classified according to the disruption root cause, as defined in [2,27]. This led to the following classification (relative occurrence in parentheses):

DL (50%): L-mode and H-mode disruptions occurring at high plasma density ('density limit') [28,29]. This was often accompanied by the development of a MARFE (a plasma edge phenomenon characterized by low local temperature compensated by high plasma density [30]) and a peaked current profile.

IMP (11%): Disruptions induced by a radiative collapse due to too high an impurity content.

NTM (7%): Disruptions due to the presence of a quasi-stationary or short-living neoclassical tearing mode (NTM).

ACC (12%): Disruptions caused by accumulation of high-Z material in the plasma core.

LON (2%): Modes excited by error fields at low plasma density ('low n_e'), typically locked at their onset.

RU (9%): Disruptions occurring during the current ramp-up phase (or at the early stage of the flat-top), induced for example by excessive gas puff.

NBIOFF (6%): Similar to DL, but accompanied by the switching off of the auxiliary NBI heating modules.

MIX (3%): Complex cases in which multiple root causes were identified.

Fig. 3 shows operational diagrams of the internal inductance l_i vs. q_{95}. Both parameters were calculated at the initiation of mode deceleration ($t = t_\mathrm{slow}$, Fig. 3a) and at the onset of the major disruption ($t = t_\mathrm{disr}$, Fig. 3b), for the cases ROT and ROT→LM. Entries within the diagram are colour-coded by disruption class. The ratio l_i/q_{95} is associated with the free energy available to drive the island growth [31]. Disruptions occurring at high plasma density can be roughly separated from the remaining classes by the $l_\mathrm{i} = 1.3$ line. In fact, the separation is already noticeable in a similar diagram constructed from data at about 0.5 s before the onset of mode deceleration, at a slightly lower value of $l_\mathrm{i} \approx 1.1$. Note that, for the DL and NBIOFF cases, the range of l_i shifts between t_slow and t_disr by $\approx 15\%$. Entries below the separation line undergo, on average, minor shifts within the parametric space. This observation is in accordance with the assumption that entries within the DL and NBIOFF group are current-driven instabilities. Increasing current profile peaking might serve as a source of free energy for the modes within these groups, thus progressively approaching the disruptive state. It is worth noting that different disruption root causes can affect the locking dynamics differently. Therefore, at times we will discuss the mode braking details in the context of the disruption class.

3.3 Collection and validation of experimental data

We now briefly present some details about the used diagnostics and characteristics of the data for the main variables in the database.
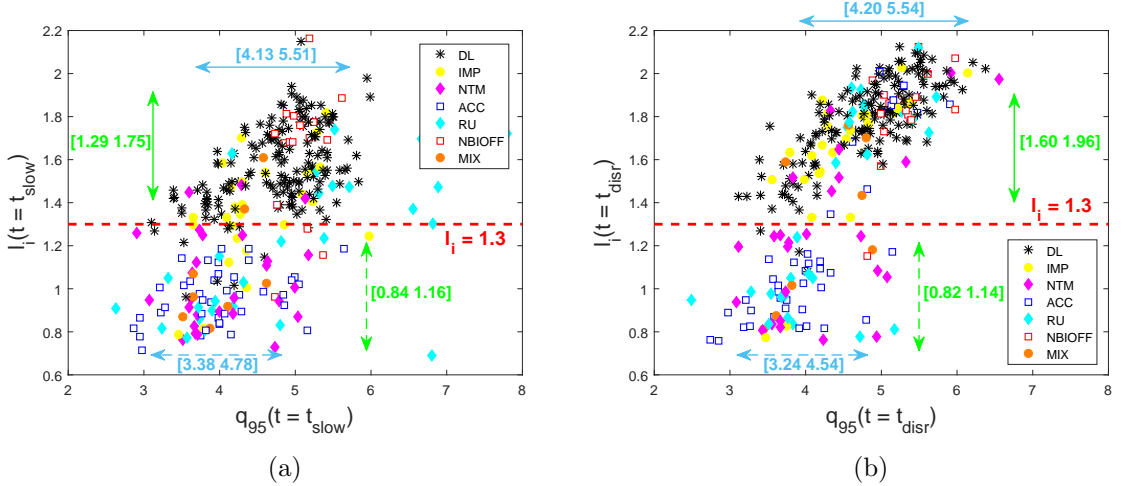
Figure 3: $l_i(q_{95})$ diagrams for ROT and ROT→LM entries obtained (a) at the mode deceleration initiation (t_{slow}) and (b) at the disruption onset (t_{disr}). Note the distinct shift of the range of l_i for the groups of disruptions occurring at high plasma density.

3.3.1 Mode frequency and amplitude

A toroidal array of Mirnov coils located at the AUG outer midplane was used to detect the perturbed field $\tilde{\mathbf{B}}$ associated with the MHD modes. Spectrograms, with a frequency resolution $\Delta f = 0.4$ kHz and temporal resolution $\Delta t = 2.5$ ms, allowed to track the experimental mode frequency ω_{exp} and amplitude (in T/s, converted to T by dividing by the mode frequency [17]). The initial rotational frequency ω_0 was defined as the maximum of the tracked frequency preceding the mode deceleration.

3.3.2 Mode structure

Mode poloidal and toroidal numbers were derived by analysis of signals from poloidal (m) and toroidal (n) Mirnov coil arrays, using either the phase fitting method or by performing the short-time Fourier transform and analysis of the cross-phase. About 50% of the initially rotating modes were of $(m/n)_{ini} = 3/1$ structure, followed by $\approx 42\%$ $(m/n)_{ini} = 2/1$ and $\approx 6\%$ $(m/n)_{ini} = 4/1$ modes. Other mode structures ($(m/n)_{ini} = 3/2, 5/1$) were present in less than 2% of the cases.

3.3.3 MHD equilibrium reconstruction

For the modes locking during the flat-top phase (67%) of the discharge, a constraint on the central value of the safety factor was set, $q_0 = 1$, in correspondence with the typical current redistribution during this discharge phase. The CLISTE equilibrium code [32] performed the fit of the flattest possible current profile while posing a regularization condition (consisting of keeping the curvature as low as possible) on the parametrized measured signals. The resulting equilibrium profiles are expected to be more realistic compared to the standard reconstructed profiles without constraints on q_0. Note that about 7% of the locking modes occurred in the current ramp-up phase and 26% during ramp-down.

The position of the rational surface of interest retrieved with an equilibrium code was compared with ECE measurements for a selected discharge [17]. A reasonable agreement was found between the equilibrium output and the location of the phase jump and minimum of the FFT amplitude from the ECE measurements.
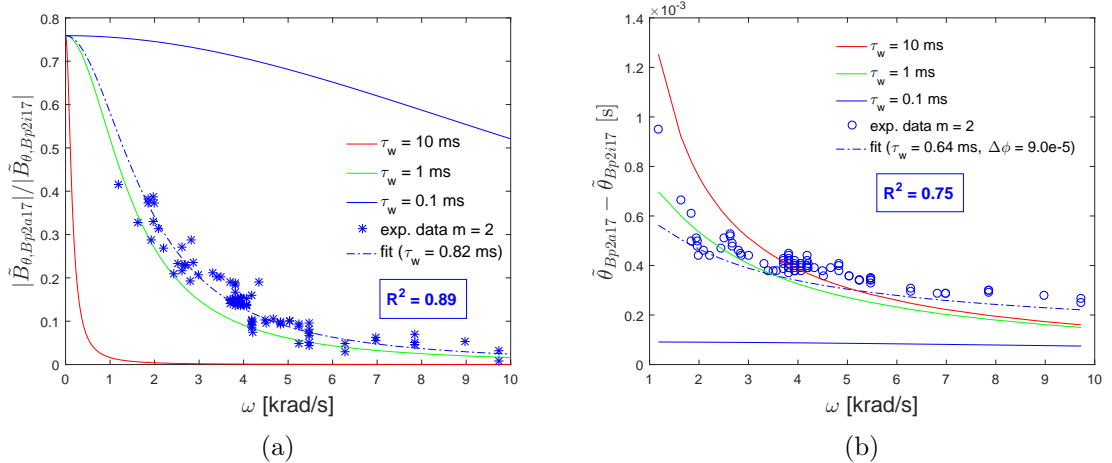
Figure 4: (a) Attenuation of the absolute value of the poloidal component of the mode field, after passing through the vessel wall. Solid lines show examples of theoretical curves, calculated with (37) for various τ_{w} ($m = 2$), considering the actual geometrical configuration of the coils. The best fit of the analytical formula to the experimental data yielded $\tau_{\mathrm{w,att}} \approx 0.82$ ms. (b) The fit of the phase shift between the mode field components yielded $\tau_{\mathrm{w,phase}} \approx 0.64$ ms ($m = 2$).

3.3.4 Resistive wall time

For the AUG vacuum vessel, (6) yields the theoretical value $\tau_{\mathrm{w,th}} = 25$ ms ($\sigma_{\mathrm{w}} = 10^7 \; (\Omega m)^{-1}$, $r_{\mathrm{w}} \approx 0.8$ m, $b \approx 0.005$ m). Since this parameter is fundamental for the model application, an experimental technique to determine it was used as well. In particular, the frequency-dependent attenuation of the mode field due to the vacuum vessel wall was calculated using (37) in Appendix A. This was based on measurements by magnetic sensors located on both sides of the wall, at the same toroidal angle and approximately the same poloidal angle (displacement of the coils along the poloidal coordinate was $\Delta\theta = 0.0314$ rad). The sensors are located at the low-field side, midplane. The phase shift was calculated from a similar expression. Data averaged over five discharges with a single 2/1 mode were used to experimentally determine the ratio. The data were fitted to (37) (see Fig. 4a) and the best fit was obtained for $\tau_{\mathrm{w,att}} \approx 0.82$ ms. Similarly, the phase difference between the signals acquired with the same pair of coils was measured and fitted with the corresponding analytical expression. Apart from τ_{w}, a phase shift $\Delta\varphi$ was added as a free fit parameter, since the integrated signals from the coils could be phase-shifted due to the hardware integration through the raw signal processing. Furthermore, the displacement of the coils along the poloidal coordinate $\Delta\theta$ was considered. The best fit yielded $\tau_{\mathrm{w,phase}} \approx 0.64$ ms (see Fig. 4b).

The construction of a frequency-dependent function of the field attenuation and phase shift associated with single locking modes can be considered as a convenient approach to deduce properties of a single conducting structure of interest in which helical mirror currents are driven. An average value $\bar{\tau}_{\mathrm{w}} = 0.73$ ms of $\tau_{\mathrm{w,att}}$ and $\tau_{\mathrm{w,phase}}$ was thus used in applications of the mode locking model. This value is clearly very different from $\tau_{\mathrm{w,th}} = 25$ ms, admittedly calculated under the highly idealized assumption of a cylindrical shell of constant thickness. This discrepancy will be the subject of further study.

3.3.5 Island width

The width of magnetic islands was estimated from magnetic sensor data, measuring the poloidal component $\tilde{B}_\theta$ of the perturbation magnetic field, as well as the magnetic equilibrium,

11

using the following expression [18]:

$$w = 4\sqrt{\left.\frac{q r_{\mathrm{s}} |\tilde{B}_r|}{m q' B_\theta}\right|_{r=r_{\mathrm{s}}}}.\tag{21}$$

Here, (34) (specifically (36)) in Appendix A was used to calculate the radial component $\tilde{B}_r(r_{\mathrm{s}})$ of the magnetic field at the rational surface, from the data of the poloidal component $\tilde{B}_\theta(r_{\mathrm{c}})$ measured at the coil position ($r = r_{\mathrm{c}}$). As a cross-check, the island width obtained from the magnetic measurements (w_{mag}) was compared with the ECE data contour plot (w_{ECE}) for a selected discharge experiencing a large mode. Estimation of w_{ECE} suffers from uncertainties due to imperfect flattening of the temperature within the island region. It should thus be considered as an upper limit of the experimental mode width. It was found that w_{mag}, corrected for the effect of toroidicity (see (45)), was in good agreement with w_{ECE}.

3.3.6   Momentum confinement time

In case of auxiliary heated AUG discharges, the experimental input needed for the calculation of τ_{M0} was obtained with individual runs of the TRANSP code [33]. Out of the ROT and ROT→LM cases, only 139 discharges could be processed with TRANSP due to occasional absence of experimental data. The calculated τ_{M0} was compared to τ_{E0}, both estimated at the same temporal point in the instability-free part of the discharge preceding the onset of mode locking. The mean of the $\tau_{\mathrm{M0}}/\tau_{\mathrm{E0}}$ was calculated to 1.09 ± 0.57. Therefore, in case of absence of experimental data necessary to calculate τ_{M0}, a value of $1.09\,\tau_{\mathrm{E0}}$ was used. During transient phases of the discharge, the confinement times should take into account the temporal derivative of the plasma energy or angular momentum, i.e.

$$\tau_{\mathrm{E0}} = \frac{W_{\mathrm{th}}}{P_{\mathrm{tot}} - \frac{\mathrm{d}W_{\mathrm{th}}}{\mathrm{d}t}},\tag{22}$$

with P_{tot} the total power input and W_{th} the plasma thermal energy, and

$$\tau_{\mathrm{M0}} = \frac{L_\phi}{T_{\mathrm{IN}} - \frac{\mathrm{d}L_\phi}{\mathrm{d}t}}.\tag{23}$$

We will refer to these expressions as 'dynamic' confinement times. However, $\mathrm{d}L_\phi/\mathrm{d}t$ could not always be evaluated due to signal discontinuities. In that case the 'static' $\tau_{\mathrm{M0}} = L_\phi/T_{\mathrm{IN}}$ was used. A comparison of calculated dynamic and stationary τ_{M} can be found in Figs. 6b,8b. It can be seen that during the transient discharge phase, $\tau_{\mathrm{M}}(\mathrm{dynamic}) \sim (0.5\text{-}0.9)\tau_{\mathrm{M}}(\mathrm{static})$. Furthermore, we note that the temporal evolution of τ_{M} and τ_{E} can differ substantially during discharge transient phases.

3.3.7   Plasma density

The electron density n_{e} at the rational surface of interest was calculated from Thomson scattering (TS) measurements. If those were unavailable, or if there were less than two TS data points during the mode duration, data from the DCN interferometer were used instead, which views the plasma region along a line-of-sight (LoS) at a normalized radius $r/a \approx 0.8$. In case the interferometer data were suffering from fringe jumps, the density was calculated during the previous available time point without fringe jumps. We note that in most cases this point was separated from the locked mode onset time by a short temporal interval, it is thus reflecting the plasma density conditions in the particular LoS plasma shortly before the onset of the transient discharge period.

3.3.8 Parameter ranges at locking onset

The period 2012–2016 covers a broad range of operational conditions and plasma parameters in AUG. In addition, the temporal evolution of the growth of the instability for the ROT and ROT→LM database entries can be very different from case to case. There are instabilities that grow explosively and lock immediately (Fig. 5, left), others are of a quasi-stable nature (Fig. 5, right), etc. Tab. 3 shows the extent of the parameter space in which the mode locking model was applied during this work. For various key parameters calculated at the onset of mode deceleration, the range across the database is presented in the format median(x)-MAD, **median(x)**, median(x)+MAD, where MAD is the median absolute deviation. Confinement times were deduced shortly before the mode onset and γ was obtained by fitting the analytical mode growth formula (9) to the experimental data. In multiple cases, γ was observed to vary during the period of mode rotation.

t_{ROT} is defined as the time between the onset and decay of the rotating mode. It has a particularly broad and skewed distribution in the database, with a median of 21 ms and an average of 135 ms. Often, rotating modes exhibited a quasi-stationary phase during their existence. Tab. 4 presents t_{ROT} for the various disruption classes. The shortest rotating mode durations are associated with the modes driven unstable at high plasma density, while the longest modes tend to be NTMs. Particularly for this disruption class, monitoring of the rotating phase can be beneficial, as it expands the temporal window for disruption avoidance significantly. On the other hand, maximum *locking* phase durations were of the order of tens of milliseconds. Modes decelerating during the plasma flat-top phase had the longest locking durations (with an average value of 33 ms and median 10 ms). The distribution of the locking durations in the ramp-down phase was narrow, peaking at ≈ 10 ms. The ramp-down phase typically shows a strong variation of plasma parameters, particularly in case of an emergency ramp-down initiated by the plasma control system. Fast current density redistribution (supported, for example, by development of a cold plasma edge) might accelerate mode locking and pose a rather strict upper limit to the locking phase duration. The DL database entries were mostly of $\omega_0/2\pi < 4$ kHz. Modes of higher $\omega_0/2\pi$ belonged mainly to the ACC, NTM and MIX categories. The parameter f_{M} in (4), accounting for the degradation of the momentum confinement, was not determined, as this would require modelling the momentum diffusion during the mode growth.

The model for mode locking used in this work was derived for cylindrical plasmas. However, modes within the database typically lock in a diverted plasma configuration. The actual mass undergoing braking is thus underestimated if the plasma minor radius given by CLISTE is used in the mode equation of motion. To compensate partially this effect, we used the effective minor radius a_{eff}, obtained by forcing the plasma shaping factor $S = q_{95}/q_{\mathrm{cyl}} = 1$ ($q_{cyl} = 5a^2 B_{\mathrm{t}}/R_0 I_{\mathrm{p}}$) [34], yielding

$$a_{\mathrm{eff}} = \sqrt{\frac{q_{95} R_0 I_{\mathrm{p}}}{5 B_{\mathrm{t}}}}. \tag{24}$$

This leads to a better representation of the braking mass in shaped plasmas. As $a < a_{\mathrm{eff}}$, the aspect ratio reduces and consequently the neoclassical transport effects amplify, but this is not considered in the model for mode deceleration that is employed here.

4 Application of the model for mode locking

4.1 Theoretical evaluation of the locking bifurcation condition

In applying the mode locking model outlined in Sec. 2 to the modes observed in our database, the condition (18) for the locking bifurcation was first investigated. Tab. 5 lists the minimum $\omega_{0,\mathrm{min}}/2\pi$ for which this condition was satisfied. About 59% of the $m = 2$ locking modes and

$\beta_{\rm p}$	W (MJ)	H98	$\tau_{\rm E0}$ (ms)	$\tau_{\rm M0}$ (ms)
0.22, **0.35**, 0.48	0.05, **0.11**, 0.17	0.34, **0.56**, 0.78	39, **57**, 75	34, **53**, 72

$n_{\rm e}(r_{\rm s})$ ($\times 10^{19}$ m^{-3})	$\tau_{\rm w}$ (ms)	$I_{\rm p}$ (MA)	$B_\theta(r_{\rm s})$ (T)	$B_{\rm t}$ (T)
4.0, **6.1**, 8.2	**0.73**	0.67, **0.78**, 0.89	0.33, **0.36**, 0.39	2.5, **2.5**, 2.5

$T_{\rm NBI}$ (Nm)	q_{95}	$l_{\rm i}$	a (m)	κ
2.2, **3.9**, 5.6	4.2, **4.7**, 5.2	1.2, **1.4**, 1.6	0.50, **0.51**, 0.52	1.5, **1.6**, 1.7

$r_{\rm w}/a$	$\omega_0/2\pi\vert_{2/1}$ (kHz)	$r_{\rm s}/a\vert_{2/1}$ (LFS)	$R_{\rm geo}$ (m)	$\delta_{\rm l}$
1.8, **1.8**, 1.8	1.6, **2.4**, 3.2	0.62, **0.72**, 0.82	1.6, **1.6**, 1.6	0.33, **0.35**, 0.37

$1/\gamma$ (ms)	$\omega_0/2\pi\vert_{3/1}$ (kHz)	$r_{\rm s}/a\vert_{3/1}$ (LFS)	$t_{\rm ROT}$ (ms)	
1.0, **33**, 64	1.2, **2.0**, 2.8	0.87, **0.91**, 0.95	5, **21**, 37	

Table 3: Ranges of parameters x in the database, retrieved at $t = t_{\rm slow}$, presented in the format median(x)-MAD, **median(x)**, median(x)+MAD, where MAD is the median absolute deviation. $\beta_{\rm p}$ is the poloidal beta, $R_{\rm geo}$ is the geometrical radius of the torus, κ the plasma elongation, W the total plasma stored energy, $\delta_{\rm l}$ the lower triangularity, B_θ the poloidal field component and $B_{\rm t}$ the toroidal field.

Disruption class	DL	IMP	NTM	ACC	RU	NBIOFF	MIX
Mean	13	13	99	69	63	13	178
Median	93	45	460	113	111	59	433

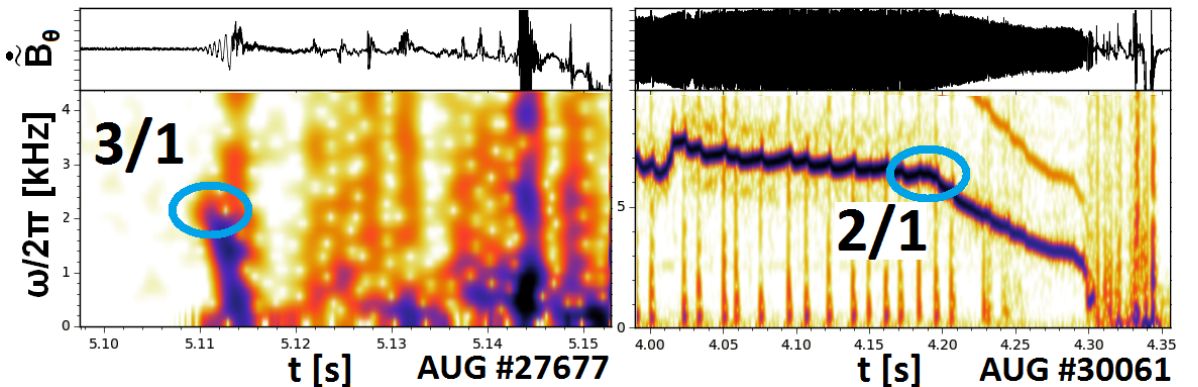Table 4: Mean and median of $t_{\rm ROT}$ (ms) within each disruption class.

Figure 5: Examples of ROT and ROT→LM database entries: immediately locking radiation-driven mode near the density limit (left), quasi-stable NTM (right). Points marking the initiation of the mode deceleration are encircled.

m	2	3	4
$\omega_{0,\min}/2\pi$ (kHz)	2.23	3.35	4.47
$\omega_0/2\pi > \omega_{0,\min}/2\pi$	59%	20%	–

Table 5: $\omega_{0,\min}/2\pi$ calculated for different poloidal mode numbers. The last row shows the number of locking modes for which the condition for mode bifurcation is fulfilled.

20% of the $m = 3$ modes had an initial rotational frequency exceeding $\omega_{0,\min}$, thus exhibiting a locking bifurcation. For the remaining cases—a substantial fraction—the point of locking bifurcation, i.e. the critical mode width for locking (Eqs. (15) and (16)), was not defined. Within the scope of the model, these modes should thus decay continuously in frequency. In the absence of an estimate of the critical mode width where the locking bifurcation takes place, our definition of the dynamic critical mode width breaks down. This will become important in Sec. 4.3.

Next, the minimum w/a for the existence of real solutions of the stationary form of (11) was evaluated for all concerned discharges. On average, the condition given by (12) was satisfied when $w/a \geq 11\%$.

4.2 Reconstruction of experimental braking curves

We next discuss reconstruction of experimental braking curves for the discharges in the database by solving the mode equation of motion (11) numerically. Both the case of plasma bulk breaking ('co') and island deceleration ('de') were considered as those represent the extreme braking scenarios. The temporal variation of the input parameters was taken into account, with the factor A_{co} (see (7)) or A_{de} (see (8)) a function of time. τ_{M} was obtained by integration of the concerned parameters over the full plasma radius. The experimentally obtained island widths $w/a(t)$ were smoothed and fitted with an analytical function of the form (9). In a number of cases, the best fit yielded $\eta < 1$. The fitted function was used to extrapolate $w/a(t)$ to a point of complete mode locking. In case of multiple (coupled) modes decelerating simultaneously, the mode with the strongest field was selected for reconstruction of the braking curve.

Out of the about 220 plasmas with initially rotating modes that were suitable for further analysis using the mode locking model, the braking curve could be integrated for 103 discharges. For the other cases, there were various reasons why $w/a(t)$ could not be fitted by the function (9), e.g. because a minor disruption took place during the deceleration phase, or due to a wildly fluctuating temporal evolution, or because the fit was of insufficient quality ($R^2 \lesssim 0.8$).

In a number of discharges, the calculated amount of decelerating torque was not sufficient to reproduce experimental braking curves (a similar observation was reported in [35]). In such cases, the mode locking model used here allows matching experimental and theoretical curves by increasing the parameter f_{M} in (4), i.e. allowing for large plasma momentum losses due to the mode itself. The value of f_{M} has to lead to a rough match between the experimental momentum confinement time in the locked state and that predicted by (4). Alternatively, the experimentally observed mode width may be increased with a factor f_{w}, yielding a modified mode equation of motion:

$$\frac{\mathrm{d}\omega}{\mathrm{d}t} = \frac{\omega_0}{\tau_{\mathrm{M0}}} - \frac{\omega(1 + f_{\mathrm{w}} f_{\mathrm{M}} w/a)}{\tau_{\mathrm{M0}}} - A\left[f_{\mathrm{w}} \frac{w}{a}(t)\right]^4 \frac{\omega \tau_{\mathrm{w}}}{(\omega \tau_{\mathrm{w}})^2 + m^2}. \tag{25}$$

Note that in the wall force term (last term on the right-hand side) the multiplication factor makes an important contribution, with a factor f_{w}^4. This effect is dominant with respect to the influence of f_{w} on decreasing the plasma momentum confinement (second term on the

right-hand side). While setting $f_M \gg 1$ may correspond to a physically plausible scenario, using a factor $f_w > 1$ for the island width is a more artificial intervention. On the other hand, the value of f_w, which turns out to be discharge-specific, does provide information concerning the amount of missing torque due to the mode-wall interaction.

4.2.1 Cases with $f_M > 0$, $f_w = 1$

Assuming first that $f_w = 1$ and by varying $f_M > 0$ to match the experimentally observed momentum confinement, good agreement was obtained between the numerical solution of the equation of motion and the experimental braking curve for 15 of the 103 initially rotating modes. An example of such a case is shown in Fig. 6 for AUG discharge #30838, during which high-Z material accumulated in the core, leading to enhanced radiation from this plasma region. Strong MHD activity was observed and the 2/1 mode of our interest appeared at $t \approx 3.52$ s (denoted by 'mode ini' in the plots). At that point the momentum confinement was relatively high ($\tau_{M0} \approx 120$ ms) and for the first tens of milliseconds after its onset, the mode remained in a quasi-stationary state. Mode braking initiated at $t \approx 3.56$ s ('lock ini'), ending at $t \approx 3.66$ s, although the mode continued to rotate at low frequency.

Plasma rotational profiles reveal that the mode was located within a region of high rotational shear. Indeed, Fig. 6c points out that deceleration started with the island, reaching the plasma centre only at a later time. The dynamic τ_M suggests that the plasma angular momentum content started to drop shortly before the mode onset (the input torque density, not shown, was roughly uniformly distributed during the mode duration). This may have been caused by an MHD mode that appeared shortly before the examined 2/1 locking mode. This MHD mode was recognisable in the spectrogram during the temporal interval $t \approx 3.487$–3.507 s, with a decaying amplitude and braking from $\omega_0/2\pi \approx 5.6$ kHz to 4.8 kHz before it disappeared. Growth of the 2/1 mode of interest initially occurred in a nonlinear fashion, reaching a saturated width of $w/a \approx 17\%$ at $t = 3.575$ s. After that, the mode started to grow exponentially. In both phases of the mode growth, (9) was fitted to the experimental curve, separately to the two growth segments. The final data vector representing the mode width temporal evolution, considered for the numerical integration of the mode equation of motion, was thus composed of the two mode growth phases along the distinct temporal intervals.

As the mode grew towards saturation, τ_M was first affected only mildly, but then started to decrease noticeably during the phase of exponential mode growth (Fig. 6d, rightmost arrow). f_M was set to a non-zero value only at the start of the braking phase, accounting for the influence of the mode on the rate of momentum redistribution. Initially, the $q = 2$ surface was located at $r_s/a \approx 0.82$, shifting to $r_s/a \approx 0.75$ by the end of the locking phase, i.e. a change of about 10%. In [9], a dependence of f_M on r_s/a was suggested, but we kept f_M constant for the numerical solution.

Fig. 6a displays the experimental and reconstructed braking curves. An agreement between the two curves for the case of full plasma column braking was obtained when $f_M = 17$. For the decoupled island braking, setting $f_M = 9$ resulted in the agreement with the experiment. At the end of the locking phase, w/a had grown to about 36%, which can be substituted in (4) to predict the decrease of τ_M. Using the dynamic formula for the experimental confinement time τ_M, a decrease from about 90 to 10 ms was observed (initial data point read at the mode onset, see Fig. 6b). In case of the static τ_M, the decrease happens from 120 ms to ≈ 12 ms. Those final values of $\approx 10 - 12$ ms are in reasonable agreement with that predicted by (4) for $f_M = 17$ (≈ 17 ms). For $f_M = 9$, the predicted drop in τ_M (≈ 28 ms) overestimates the experimental situation.

For the other 14 cases for which the experimental braking curve could be reconstructed with $f_w = 1$, $f_M > 0$, the manually obtained value of the parameter f_M was found to lie between 1 and 18, decreasing the momentum confinement time by a factor of $\lesssim 6$ at locking. In Fig. 7, the parameter f_M is plotted against the discharge-specific ratio τ_{M0}/t_{lock}. The general

rising trend is in accordance with physical arguments that were already mentioned, i.e. that correction of the momentum confinement losses due to the mode becomes increasingly critical as the ratio of momentum redistribution time to locking time rises. As a rule of thumb, the model is able to reproduce the experimental braking curve, such that $\omega_{\text{exp}}(t) \approx \omega_{\text{int}}(t)$ during the entire braking phase, when $\tau_{\text{M0}}/t_{\text{lock}} \lesssim 2$.

4.2.2 Cases with $f_{\text{M}} \gg 0$ or $f_{\text{w}} > 1$

We next proceed to plasmas where it was not possible to adjust f_{M} such that both the numerically integrated braking curve and the predicted drop in τ_{M} agreed with the experiment. This observation is reported in 88 out of the 103 cases. Furthermore, in $\sim 35\%$ of the 103 tested cases, the discrepancy between the experimental and predicted locking duration for both 'co' and 'de' scenarios was overestimated by a factor of $1.3 - 2$. The missing braking torque was compensated by setting either $f_{\text{w}} > 1$ or $f_{\text{M}} \gg 1$ (or a combination of both, see below). An example of one of those cases is examined in the following.

In Fig. 8 an initially rotating mode occurring during the AUG discharge #28227 is shown. We inspect the discharge details to examine the potential source of the above mentioned discrepancy. The disruption took place due to a locked mode that appeared as a consequence of high density and an impurity influx, according to a scenario similar to the H-mode density limit presented in [29]. More specifically, the discharge entered a transient period at around 6 s. At this time, the Greenwald fraction reached $n_{\text{e}}/n_{\text{GW}} \approx 0.96$ and l_{i} started to gradually increase, while the thermal stored energy W_{th} started to decrease. Slightly later, an NBI source tripped briefly (see the dip in the corresponding time trace in Fig. 8b at $t \approx 6.05$ s), which could have led to a redistribution of the torque input density. Due to divertor detachment, a region of cold plasma, presumably a MARFE, developed early in the transient phase. This cold plasma region started to shift poloidally at around 6.105 s. At the same time, the equilibrium reconstruction suggests that the plasma separatrix moved slightly towards the torus inner wall, which may have led to the material erosion (the measured tungsten concentration in the plasma has risen). A cold dense region is recognized to shortly stabilize close to the midplane at the inner part of the torus. In addition, the plasma appears to have briefly entered and left the H-mode during the transient period, the second time at $t \approx 6.112$ s. A 'cold edge', featuring highly peaked current density profiles, developed progressively, driving a 3/1 mode unstable at $t \approx 6.145$ s, which started to decelerate immediately. The mode was located at a normalized radius $r_{\text{s}}/a \approx 0.91$ and it grew within 7 ms from $w/a \approx 3\%$ to $w/a \approx 14\%$. Rotation profiles (not shown) reveal a large and fast variation of the central plasma rotation. Changes were also observable in T_{e} and T_{i}, with the latter gradually decreasing and the former increasing. The initially rotating mode was followed by a rise of the locked mode signal (Fig. 8d). It is thus probable that the toroidal rotation of the plasma column changed rapidly, at least in the vicinity of the rational surface. Note that in this particular case, the line-integrated plasma density was retrieved from the DCN interferometer data. These suffered from a fringe jump at $t \approx 6.108$ s, presumably due to displacement of the cold region. This was the last temporal point at which the density was calculated, therefore the plasma density was kept constant at this value in the numerical integration of the braking curve. However, Fig. 8a clearly shows that, for $f_{\text{M}} = 0$ and $f_{\text{w}} = 1$, the integrated curves in both the 'co' and 'de' scenarios do not correspond to the experimental curve, the rotational frequency is severely overestimated ($\omega_{\text{exp}} \ll \omega_{\text{int}}$).

In Fig. 8c, $f_{\text{M}} \gg 0$, or $f_{\text{w}} \gg 1$, or a combination of both was adopted in the attempt of the braking curve reconstruction. Only the 'co' scenario is shown here, first for $f_{\text{w}} = 1$ and $f_{\text{M}} \gg 1$. The value $f_{\text{M}} = 110$ yielded the best approximation to the data points, but failed to reproduce the frequency decay to a locked state that was observed experimentally, instead showing asymptotic behaviour. These settings of f_{M} and f_{w} predict a decay of τ_{M} from 17 ms ($\approx \tau_{\text{M0}}$) to ≈ 1 ms, i.e. decreasing τ_{M0} by about a factor 20. However,
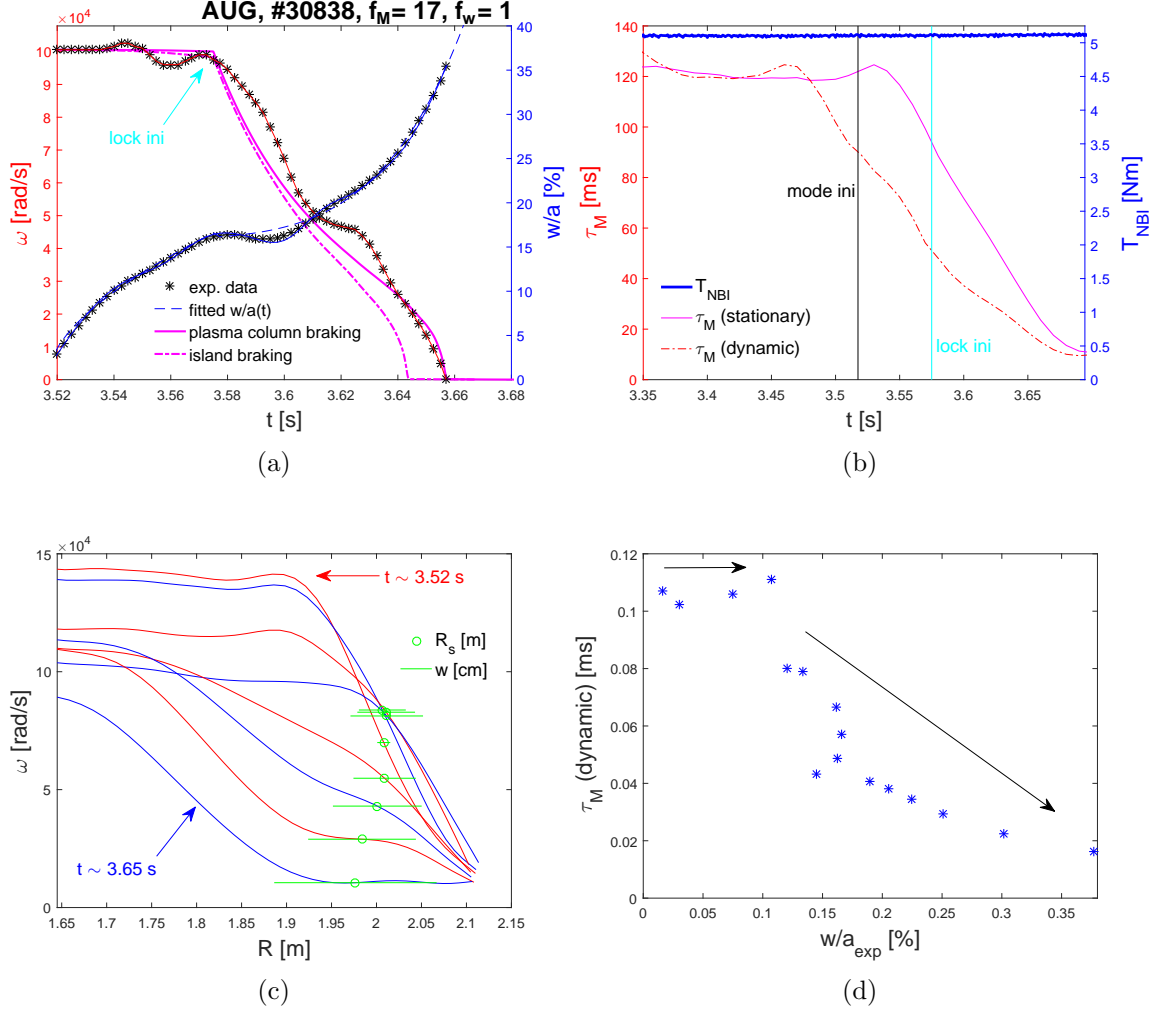
Figure 6: NBI-heated discharge #30838 with a 2/1 mode. (a) Comparison of experimental and reconstructed braking curves, both braking curves were obtained by setting $f_M = 17$. In case of the 'de' scenario this leads to underestimation of the experimental braking duration. Setting $f_M = 9$ results in matching of the 'de' scenario braking curve to the experimental data points, but the 'co' scenario overestimates the locking phase duration. Note that only the 'fitted w/a(t)' and the associated data points (visualized by black stars and bold blue line) were plotted w.r.t the right vertical axis. (b) Temporal evolution of T_{NBI} and τ_M. (c) Temporal evolution of rotation profiles. (d) Evolution of the dynamic τ_M during the mode growth.
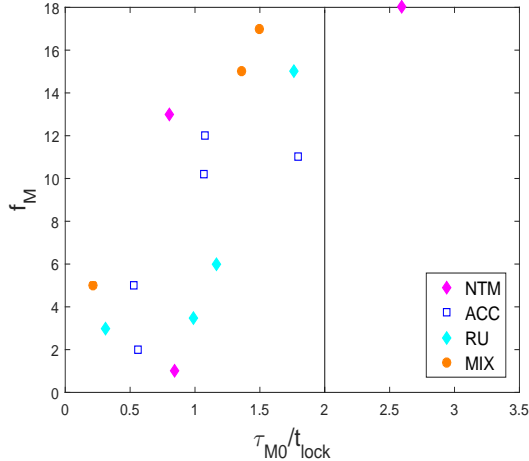
Figure 7: Parameter f_M vs. the discharge-specific ratio τ_{M0}/t_{lock}. As a rule of thumb, the mode locking model can reproduce the experimental braking curves when $\tau_{M0}/t_{lock} \lesssim 2$. Only the disruption classes NTM, ACC, RU and MIX are present in the plot.

experimental data suggest that the momentum confinement time at the end of the transient phase was about 11 ms. It should be noted that the calculation of τ_M relies on the knowledge of the rotation profiles, whereas in case of this discharge the $\omega(r)$ profiles could suffer from considerable uncertainties during the transient phase. In a next attempt, the values $f_w = 3.0$ and $f_M = 0$ were chosen. In this case, the reconstructed braking curve decays to locking at the experimentally observed time, but the details of the experimental braking curves are not captured, with $\omega_{\exp} \ll \omega_{\text{int}}$. Finally, for $f_w = 2.5$ and $f_M = 35$ a satisfactory braking curve was obtained. However, with these settings the predicted final momentum confinement time is $\tau_M \approx 2$ ms, i.e. about a factor 9 smaller than τ_{M0}, significantly underestimating the experimental value. We therefore conclude that with this combination of $f_w > 1$ and $f_M \gg 1$, the momentum losses of the plasma column are not dominated by the braking mode within the scope of the model. This is discussed in more detail in Sec. 6.

4.2.3 Relation of t_{lock} and f_w with plasma parameters and disruption classes

For all 103 initially rotating modes, braking curves were reconstructed such as to match the experimentally observed duration t_{lock} of the locking phase with that obtained from the integrated braking curve. In case this match could not be achieved using $f_M > 0$ and $f_w = 1$, with the additional requirement of consistency with the experimental confinement time at the locking, also $f_w > 1$ was applied. Analysis of the 103 discharges yielded average values $\bar{f}_{w,\text{co}} = 1.5$ (median 1.2) and $\bar{f}_{w,\text{de}} = 1.2$ (median 1.0). In the following, we focus on the 'co' scenario, involving plasma column braking.

To further examine the potential dependence of the experimental locking duration on the plasma parameters, the Pearson correlation across the *full set* of 103 discharges was calculated between t_{lock} and various parameters x at braking initiation. The correlation between t_{lock} and the total change Δx of x over the entire period of braking was determined as well. In the following, we refer to the absolute value of the correlation.

A strong correlation was found between t_{lock} and the change in the pressure-dependent parameters ($\Delta\beta_p$, ΔW_{th}). In most cases β_p decreased during the braking phase ($\Delta\beta_p < 0$), which might be mainly associated with a decrease in the plasma kinetic pressure. This could be due to a drop in the plasma temperature, potentially caused by the mode and localized plasma cooling. In turn, this may influence the mode velocity through the electron
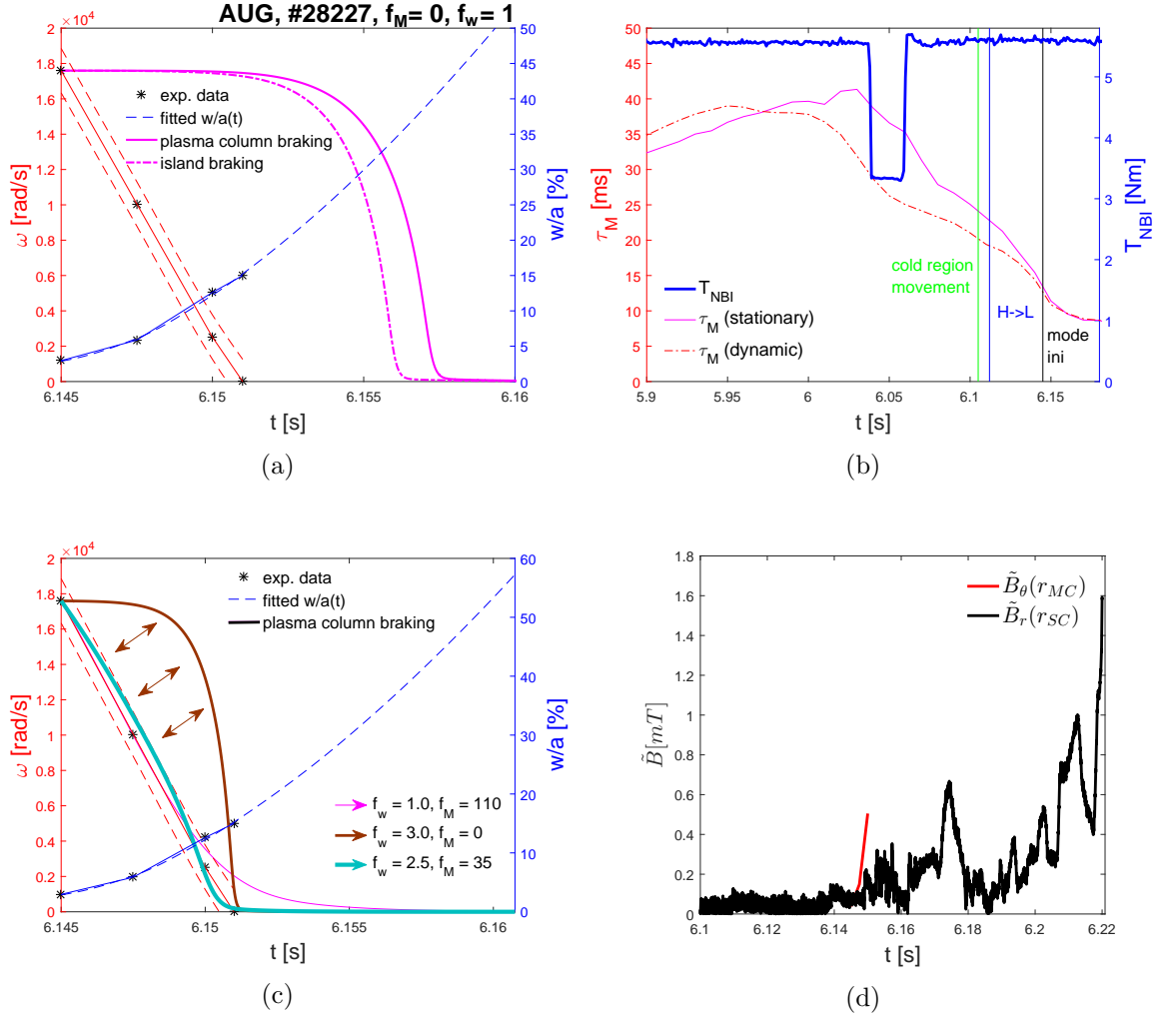
19

Figure 8: NBI-heated discharge #28227 with a 3/1 mode. (a) Comparison of experimental and reconstructed braking curves. (b) Temporal evolution of T_{NBI} and τ_{M}. (c) Attempts to reconstruct the experimental braking curve by setting $f_{\mathrm{M}} \gg 1$ and/or $f_{\mathrm{w}} > 1$. Only a combined adjustment of both factors allows to reproduce the experimental braking curve. (d) The locked mode field amplitude $\tilde{B}_r(r_{\mathrm{SC}})$ (black bold line, measured at the saddle coil location r_{SC}) rises above the noise level at $t \approx 6.149$ s. The rotating mode amplitude $\tilde{B}_\theta(r_{\mathrm{MC}})$ starts to rise shortly before (red bold line, measured at the Mirnov coil location r_{MC}).
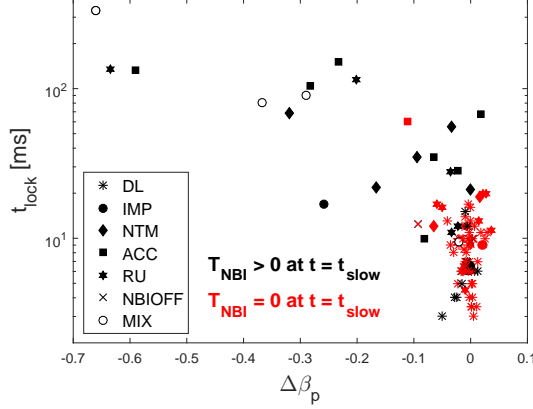
Figure 9: Experimental locking duration t_{lock} plotted against the variation in β_p occurring during the mode braking. Color coding separates $T_{\text{NBI}} > 0$ and $T_{\text{NBI}} = 0$ (both calculated at $t = t_{\text{slow}}$) cases. Note that for better data visualization the class code symbols differ from those previously displayed.

diamagnetic drift, given by

$$\boldsymbol{v}_{\text{e,dia}} = \frac{\boldsymbol{\nabla} p_{\text{e}} \times \boldsymbol{B}}{n_{\text{e}} e B^2}. \tag{26}$$

On the other hand, in case of the NBI heated discharges, the mode rotation can be dominated by the ion bulk rotation, suppressing thus the relative importance of $v_{\text{e,dia}}$. We report that t_{lock} correlated positively with T_{NBI} and also with ω_0. This observation is in accordance with the assumption that the external torque input acts as a source of plasma rotation, which can be reflected in higher mode initial rotational frequency and can lead to extended braking phase duration. Fig. 9 displays t_{lock} in the context of $\Delta\beta_p$ and resolves the cases with NBI torque input and without it at $t = t_{\text{slow}}$. The plot area can be virtually divided along $\Delta\beta_p = -0.05$. The strong correlation between t_{lock} and $\Delta\beta_p$ is preserved for cases with $\Delta\beta_p < -0.05$. Those cases are typically of long braking phase durations and with $T_{\text{NBI}} > 0$ at $t = t_{\text{slow}}$. The mode rotation can be thus dominated by the external torque input there, giving the electron diamagnetic drift mode velocity component a minor relative importance. The reason for the strong correlation between t_{lock} and $\Delta\beta_p$ can thus not be traced back to an effect of $v_{\text{e,dia}}$ alone.

We note that only a weak correlation was observed between t_{lock} and the change of pressure-dependent parameters *preceding* the locking phase (the temporal interval of interest was set 200 ms prior to the mode braking until the locking initiation). This suggests that the rate of mode momentum loss is mainly related to the variation of the plasma parameters *during* the mode locking.

A moderate correlation between t_{lock} and Δl_i, Δq_{95} and $\Delta l_i/q_{95}$ was observed. The first two parameters determine the q-profile, thus indirectly affecting the position of the resonant surface r_s. As mentioned before, the ratio l_i/q_{95} is related with the free energy available for growth of the mode. In turn, this may influence the mode growth rate, which is strongly correlated with t_{lock}.

As in the case of t_{lock}, $\Delta\beta_p$ and ΔW_{th} appear to be linked to f_w, but the correlation was relatively weak. A weak positive correlation between r_s/r_w and f_w was observed. This is somewhat counter-intuitive, since the braking force increases when the mode is located closer to the wall. On the other hand, the mode growth might also be counter-acted by currents induced in the wall. A moderately negative correlation between f_w and ω_0 was observed, suggesting a decreasing need for correcting (increasing) the mode wall torque for modes with
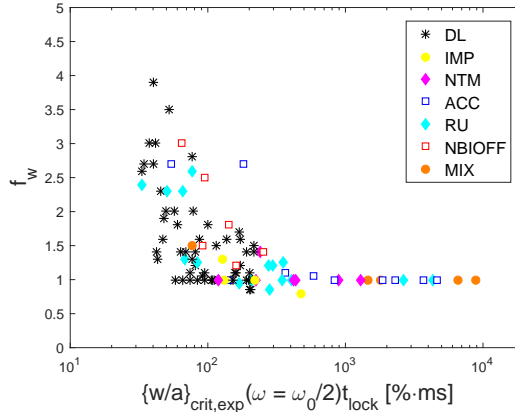
21

Figure 10: Parameter f_w vs. $(w/a)_{\mathrm{crit,exp}}t_{lock}$, indicating disruption classes. The wall torque exerted on large modes locking over long temporal intervals requires a minimum artificial increment.

higher initial rotational frequency.

A plot of f_w is shown in Fig. 10. It shows that the correction factor f_w has a tendency to decrease with the product of t_{lock} with $(w/a)_{\mathrm{crit,exp}}$. The latter is defined as the experimental island width calculated at $\omega = \omega_{\mathrm{crit}}$ (see Sec. 4.3). This means that the correction of the wall torque becomes less important for large islands with an extended braking phase. Furthermore, Fig. 10 resolves the disruption classes, suggesting that $f_w > 1$ is systematically necessary for the DL class disruptions. Recall that for this particular class, l_i varied significantly during the time between braking initiation and disruption onset (Fig. 3). As DL plasmas are likely to develop a cold edge, the resulting changes in the current profile may explain at least partially the need to correct the torque. In addition, interplay between local cooling by the mode and the presence of a cold edge might further enhance changes in the plasma momentum content.

Unfortunately, the relation between t_{lock}, f_w and the plasma density could not be examined for the full set of discharges, particularly for the DL cases.

4.3 Experimental evaluation of the locking bifurcation condition

In the following, we attempt to experimentally validate the dynamic condition for locking bifurcation given by (20) (we refer to the 'co' braking scenario only). Out of the 103 cases suitable for application of the mode locking model (and therefore for the bifurcation condition validation), the necessary condition (18) for the locking bifurcation to take place was fulfilled in 61 cases. Furthermore, the conditions $\eta \geq 1$ (mode growing linearly or faster in time, recall (9)) and $\alpha \leq 9$ (i.e. the maximum value of this parameter across the parametric scan discussed in Sec. 2.3) were satisfied for 23 out of those 61 cases. Therefore, in only 23 cases we could proceed to comparison of experimental and predicted critical island width for locking. In Sec. 4.2.1, the experimental braking curves were reproduced for f_M between 1 and 18, whereas for the rest of the discharges, the value of this parameter was undetermined. Furthermore, this parameter is not included in the definition of the dynamic locking bifurcation condition. Therefore, in evaluating the critical island width for locking, $f_M = 0$. For the purpose of further discussion, we note that equation (17) allows evaluating the critical mode frequency ω_{crit} at which a locking bifurcation takes place. In the following, using $f_M = 0$, we obtain $\omega_{\mathrm{crit}} = \omega_0/2$.

For each of the 23 cases, $(w/a)_{\mathrm{crit,s}}$ and $(w/a)_{\mathrm{crit,d,fit}}$ were *calculated* using (15) and (20), respectively. Means and medians of the calculated terms are displayed in Tab. 6. According
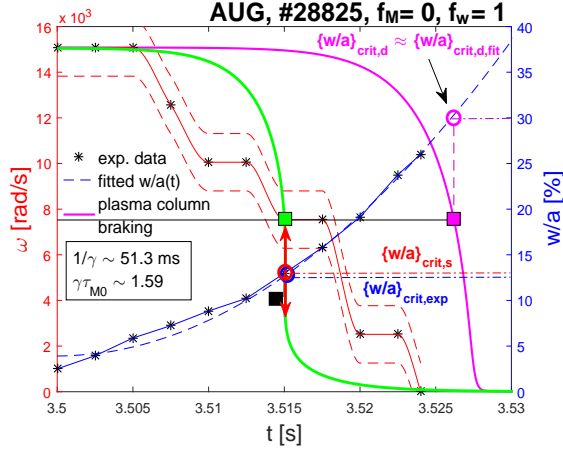
Figure 11: Experimental evaluation of the condition for mode locking (i.e. the point of locking bifurcation) for discharge #28825 (2/1 mode), with $f_M = 0$, $f_w = 1$. The green line shows the static braking curve and the double red arrow delimits the forbidden frequency range, while the magenta line corresponds to dynamic braking (recall Fig. 2a). The experimental $\omega(t)$ data points were not smoothed, the discrete data points thus reflect the temporal and frequency resolution of the spectrogram (see Sec. 3.3.1).

to the expectations, the average/median dynamic critical island widths exceed the stationary equivalents.

Furthermore, we obtain $(w/a)_{crit,d}$ from the fitted $w/a(t)$ curve at a temporal point at which the integrated braking curve decays in frequency to ω_{crit} (see an example in Fig. 11). In principle, $(w/a)_{crit,d,fit}$ and $(w/a)_{crit,d}$ should match. However, given the approximations made along derivation of equation (20) and together with that $A(t)$ was considered a function of time, whereas A is taken a constant in the definition of $(w/a)_{crit,d,fit}$ (A was calculated from plasma parameters obtained at the time of initialization of the numerical integration for the purpose of the $(w/a)_{crit,d,fit}$ calculation), $(w/a)_{crit,d,fit}$ and $(w/a)_{crit,d}$ can differ. In the example shown in Fig. 11, $(w/a)_{crit,d,fit} \approx (w/a)_{crit,d}$. Tab. 6 allows comparison of means/medians of the two critical island widths for the 23 discharges. The average effect of the two above factors results in $(w/a)_{crit,d,fit} \approx 1.2 \, (w/a)_{crit,d}$.

We note that among the 23 here discussed discharges, multiple cases required f_w to match the experimental and predicted locking duration (for example, $f_w = 1.4$ in case of the locking mode displayed in Fig. 11). Multiplication of the island width by $f_w > 1$ typically resulted in the modification of the mode growth parameters and therefore the change in $(w/a)_{crit,d,fit}$ and $(w/a)_{crit,d}$. The observed variation was, however, minor.

Last column of the table contains the experimental island width at ω_{crit}, $(w/a)_{crit,exp}$. It can be seen that the median experimental island width, calculated for the 23 cases of interest, exceeds both $(w/a)_{crit,d,fit}$ and $(w/a)_{crit,d}$ by the respective factors ~ 3 and ~ 2. We report thus that the physics elements contained in the dynamic condition for locking bifurcation are insufficient to reproduce the experiment.

Finally, the experimental island width at ω_{crit} was retrieved for all 103 discharges, regardless of whether the condition for locking bifurcation given by (18) was satisfied. With this manipulation, we can present in Tab. 7 summary statistics concerning $(w/a)_{crit,exp}$ and $f_w(w/a)_{crit,exp}$. It can be seen that the mean 'corrected' $f_w(w/a)_{crit,exp}$ is larger than its experimental uncorrected equivalent by a factor of ≈ 1.3 in the 'co' scenario and 1.1 in the 'de' scenario.

	$(w/a)_{\mathrm{crit,s}}$	$(w/a)_{\mathrm{crit,d,fit}}$	$(w/a)_{\mathrm{crit,d}}$	$(w/a)_{\mathrm{crit,exp}}$
Mean	15.5	35.8	31.1	13.7
Median	14.0	36.7	29.8	12.5
Std	6.1	9.3	9.3	6.5

Table 6: Means and medians of $(w/a)_{\mathrm{crit}}$ of interest for $f_{\mathrm{M}} = 0$, expressed as percentages. Standard deviations have been added in the last row ('Std').

Scenario		$(w/a)_{\mathrm{crit,exp}}$	$f_{\mathrm{w}}(w/a)_{\mathrm{crit,exp}}$
'co'	Mean	14.9 ± 6.9	19.6 ± 7.1
	Median	13.7	18.4
'de'	Mean	14.9 ± 6.9	16.3 ± 6.9
	Median	13.7	14.4

Table 7: Means and medians, expressed as a percentage, of $(w/a)_{\mathrm{crit,exp}}$ and $f_{\mathrm{w}}(w/a)_{\mathrm{crit,exp}}$ for 103 discharges.

5   Rotating modes triggering disruptions

At AUG, as at various other devices, a real-time locked mode signal is used as a disruption warning monitor for emergency discharge shutdown [36]. However, from Tab. 2 it follows that 27% of the modes in our database were rotating at the disruption onset. We subdivided this category of modes into two groups according to their frequency at disruption initiation. Indeed, the maximum of the wall torque occurs at $\omega \approx m/\tau_{\mathrm{w}}$. In the case of AUG, this is at $\omega/2\pi \approx 430$ Hz and $\omega/2\pi \approx 650$ Hz for $m = 2, 3$ modes, respectively ($\tau_{\mathrm{w}} = 0.73$ ms, see Sec. 3.3.4). Modes disrupting the plasma above this frequency ($\approx 25\%$ of the ROT cases) were assigned to a 'ROT-high' group, the other modes falling into a 'ROT-low' group. In the latter case, the wall torque is assumed to be weak and other forces applied on the mode (such as device error fields [15, 37]) may dominate the locking process.

In Fig. 12a, a spectrogram is shown with a disruptive, progressively growing and locking ROT-high mode. The disruption took place at about 3.715 s, at which point the mode rotational frequency was $\omega/2\pi \approx 5$ kHz. Fig. 12b displays the measured locked mode amplitude. Because of the high rotational frequency, the locked mode amplitude only barely surpassed the noise level during the last phase of the discharge. As a consequence, the warning levels for machine protection were not reached (a 'soft-stop' initiates a fast current ramp-down, while the massive gas injection (MGI) threshold activates gas filling through the disruption mitigation valves). In addition, the figure shows the disruptive locked mode amplitude $\tilde{B}_{\mathrm{LM,disr}}$ (black dashed line), calculated from a recently established scaling [3], accounting for the position r_{SC} of the saddle coils. This empirical formula allows, for a given experimental input, to estimate the locked mode amplitude at which a disruption is initiated. Throughout the mode duration, it estimates a disruptive amplitude of ≈ 0.6 mT. In dashed green, the disruptive locked mode amplitude is calculated accounting for the position of the Mirnov coils ($r = r_{\mathrm{MC}}$). In red, the poloidal field component of the mode is displayed, measured with the Mirnov coils, $\tilde{B}_{\theta}(r_{\mathrm{MC}})$, as well as $\tilde{B}_r(r_{\mathrm{MC}})$ (green) using (34). The measured value of the radial field component surpassed the predicted field intensity at the initiation of the disruption. This example demonstrates that large decelerating modes rotating at high frequencies at the disruption onset are undetected by the present AUG device protection schemes. Moreover, due to the hardware signal processing, amplitudes of the ROT-low group are attenuated. Despite growing to significant amplitudes, this attenuation might cause the machine protection to fail to react on these modes.
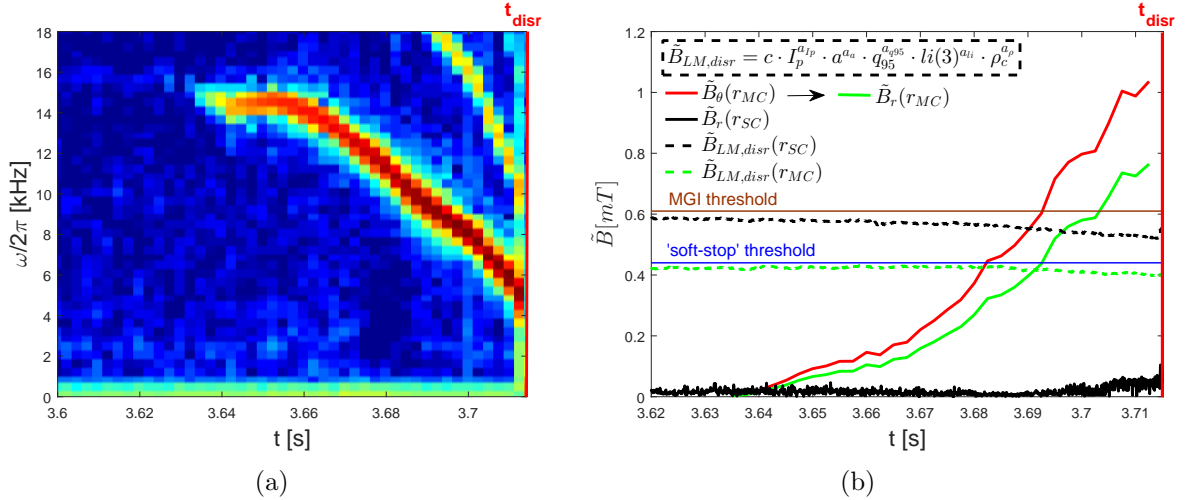
Figure 12: Discharge #32505 disrupted due to a locking 2/1 mode (coupled with a 3/1 mode). (a) A spectrogram tracks the mode's field $\tilde{B}_\theta(t)$ and $\omega(t)$. (b) Time traces of the mode field detected by the Mirnov coils ($\tilde{B}_\theta(r_{\mathrm{MC}})$, converted to $\tilde{B}_r(r_{\mathrm{MC}})$ using (34)) and the locked mode detector ($\tilde{B}_r(r_{SC})$). In addition, the disruptive locked mode amplitude $\tilde{B}_{\mathrm{LM,disr}}$ is plotted, predicted by an empirical scaling, either calculated using the position of the saddle coils (r_{SC}) or that of the Mirnov coils (r_{MC}). Also shown are the field amplitudes predefined by the device protection scheme to initiate an emergency ramp-down ('soft-stop') or open the disruption mitigation valves ('MGI').

6 Discussion and prospectives for extension of the mode locking model

The model for mode locking that was used in this study can describe two extreme scenarios of mode braking: either the mode locking is decoupled from the plasma bulk motion ('de'), or the plasma column decelerates with the mode ('co'). The evolution of the experimental rotation profiles shown in Sec. 4.2.1 suggests, however, that the actual situation might be a compromise between the two scenarios. The extent to which either scenario is a good approximation is likely related to the instantaneous mode width and the rate of the mode growth relative to the rate of momentum redistribution. In practical applications, one could estimate the critical mode width for locking and the locking duration using the two scenarios, resulting in an interval of critical locking parameters with boundaries defined by the two braking scenarios.

Degradation of the confinement properties during the discharge can occur due to multiple reasons, which can be difficult to disentangle. In some cases, setting $f_{\mathrm{M}} < 18$ and $f_{\mathrm{w}} = 1$ allowed reconstruction of the experimental braking curves, with the mode braking usually accompanying the onset of the momentum confinement deterioration (Sec. 4.2.1). In those cases, momentum confinement times at locking, predicted by (4), agreed with the experimental data points, decreasing the initial momentum confinement time by a factor $\lesssim 6$. For a number of examined locking modes, the predicted value of the momentum confinement time for $f_{\mathrm{M}} \gg 1$ was of the order of milliseconds or less. For a given constant torque density input, such low values would imply a plasma column at almost complete rest at locking. However, experimental rotation profiles often reveal a delayed deceleration of the central part of the plasma, with respect to the mode (see Ref. [8] for a similar observation in the JET tokamak).

In a substantial fraction of the cases studied here, the calculated wall torque was not large enough to reproduce the experimentally observed locking (Sec. 4.2.2). A similar observation

25

was reported in the DIII-D tokamak, hypothesized in [35] to originate from the existence of a second in-vessel conducting structure that could contribute to mode locking. The characteristic resistive time of this second structure would be an order of magnitude smaller than that of the vacuum vessel. As a result, a component of the wall torque would be introduced, reaching a maximum at comparatively higher mode frequencies, compensating for the missing braking torque. However, this model involving two resistive shells does not appear to be a suitable candidate to explain the missing torque in our observations, since the need to compensate for the missing torque only presented itself under specific discharge conditions, not universally (see below).

Within the scope of the model used in this paper, the stationary condition for the locking bifurcation is only suited for determining the critical mode width for locking when the mode grows on a sufficiently long time scale compared to that of the momentum redistribution. Therefore, in most practical applications the dynamic condition for the bifurcation should be used instead. In this paper, the dynamic bifurcation condition was restricted to certain mode growth scenarios and did not include the momentum confinement time degradation (Sec. 2.3). Validation of this theoretical condition was thus affected by those restrictions. In Sec. 4.3 it turned out that the predicted and experimental critical island widths differed substantially, possibly due to the above limitations. The dynamic condition for the locking bifurcation is a step forward in estimating the critical island widths in practical cases, but highlights the necessity to include more physical mechanisms in its definition.

The condition for the locking bifurcation was satisfied for about 60% of the 2/1 locking modes and 20% of the 3/1 modes. A substantial fraction of decelerating modes thus lack a definition of the critical island width for mode locking. For the full set of 103 discharges, normalized island widths at half of the frequency decay were thus assembled. It turned out that at this point, the islands typically extend over about 15% of the plasma radius. However, to match the experimental and numerically calculated locking durations, the modes would have to extend, on average, over about 20% of the radius for the scenario with full plasma column braking (Sec. 4.3). The critical island width in a scenario of decoupled island braking would be more compatible with the experiment.

The mode locking model used here takes into account only two forces on the mode and assumes rigid body motion, either fully coupled to or decoupled from the plasma bulk. A more detailed description of the mode locking should incorporate additional forces, such as interactions with external fields, and consider the momentum redistribution by solving the momentum transfer across the plasma [37]. On the other hand, the feasibility of such a scheme might be questioned in the context of a large database, or as a real time application during the discharge. In contrast, an advantage of the simple model used here is that it might allow to estimate locking durations and critical mode widths in real time.

One possible source of deceleration that was neglected in this work is the poloidal component of the wall force term, as the motion in this direction was assumed to be damped. However, according to Ref. [13], the associated force term component is, when evaluated with the discharge-specific parameters, one or two orders of magnitude larger than the toroidal component. Thus, identifying the circumstances under which the poloidal component of the force becomes important, could be a next step in the analysis of mode braking.

Multiple root causes can destabilize resistive instabilities and a clustering according to disruption class was recognizable in the operational diagram containing l_i and q_{95}, about half a second before the locking onset [22] (Sec. 3.2). Following the study presented here, it appears that the model can predict locking durations for disruptions falling into certain disruption classes. The model systematically fails to predict locking of initially rotating modes that are driven unstable at high plasma density and/or that are compromised by a high impurity content. In discharge #28227, where the model failed to reproduce the experimental braking curve (Sec. 4.2.2), the mode was seeded after a cold region, originally located at the vessel

inner bottom (see Fig. 13a), was detected at the inner midplane (Fig. 13b). Following a slight separatrix movement, the local vessel wall erosion could have enhanced the radiative losses, thus increasing the local density. Unfortunately, the DCN interferometers suffered from fringe jumps during the cold region development. However, the CO_2 interferometer edge channel (not routinely examined at AUG due to the high noise level and sensitivity to the external heating power and environmental conditions) shows the effect of the cold region on density (Fig. 13c). Specifically, a transient density increase can be observed, up to about 2.5×10^{20} m^{-3}, presumably owing to the corresponding line-of-sight intersecting the cold and dense region. At an increased density the plasma rotational frequency would have to decrease for the toroidal angular momentum to remain constant.

The mode equation of motion, accounting for the effect of a local particle source, e.g. caused by a MARFE, might adopt the following form:

$$\frac{d\omega}{dt} = -\frac{\omega}{n_e}\frac{dn_e}{dt} + \frac{n_{e0}\omega_0}{n_e\tau_{M0}} - \frac{\omega(1 + f_M f_w \frac{w}{a})}{\tau_{M0}} - A\left[f_w \frac{w}{a}(t)\right]^4 \frac{\omega\tau_w}{(\omega\tau_w)^2 + m^2}. \qquad (27)$$

Here, n_{e0} is the electron density at the resonant surface at the onset of braking. In case of fast ($\ll \tau_{M0}$) and large variations of the density, the first term on the right-hand side can dominate the mode slowing down, while for $dn_e/dt \approx 0$ (i.e. $n_e \approx n_{e0}$) the equation approaches its original form of (11). A test was conducted to integrate (27) in the decoupled braking scenario, at the same time mimicking the presence of a significant particle source during mode braking. A simplified model with constant dn_e/dt was applied for the rate of density increase, starting from $n_{e0} = 10^{20}$ m^{-3} at the onset of the mode deceleration and ending at a maximum density $n_{e,max} = 2.5 \times 10^{20}$ m^{-3} roughly at the end of the braking phase, in accordance with the CO_2 interferometer data. The density variation was also taken into account for calculating the parameter A_{de} from (7). Note that in Fig. 13c the density probably fluctuates due to the cold dense region moving in and out of the viewing chord, even though it is assumed to represent a particle source during the entire braking phase. The resulting braking curve is plotted in Fig. 13d (cyan dotted curve) and compared with the result from the mode equation (11) without particle source (dashed-dot magenta curve). The settings $f_M = 5$ and $f_w = 1$ were used, the former value chosen in order to match the experimentally observed decrease of the momentum confinement (Fig. 8b). It can be seen that the output of (27) agrees well with the experimental braking curve at the initial phase of braking, reducing the need to artificially increase the decelerating wall torque.

Finally, we note that, in the study presented here, about 21% of the modes leading to a disruption were rotating at the disruption onset (Sec. 5). These might go unnoticed to present machine protection systems that are based on locked mode detection. Therefore, a useful extension of disruption prediction schemes might rely on monitoring rotating mode amplitudes with additional sensors. Furthermore, the predictive power of the previously developed empirical scaling for critical amplitudes of locked modes (see [3]) could be examined for rotating modes as well.

7   Conclusions

A large database of tearing modes was assembled at AUG, contributing to plasma disruptions, under a variety of operational conditions. The database entries were classified according to disruption cause. The modes within the database either locked and contributed to the plasma disruption, or caused the disruption during their rotating phase. Characterization of the locking phase could thus provide key information for the purpose of disruption avoidance and prediction, based on the duration of the braking phase and critical mode width for locking. A simple analytical model was employed in order to describe the experimentally observed dynamics of mode braking, in particular to predict braking duration and critical
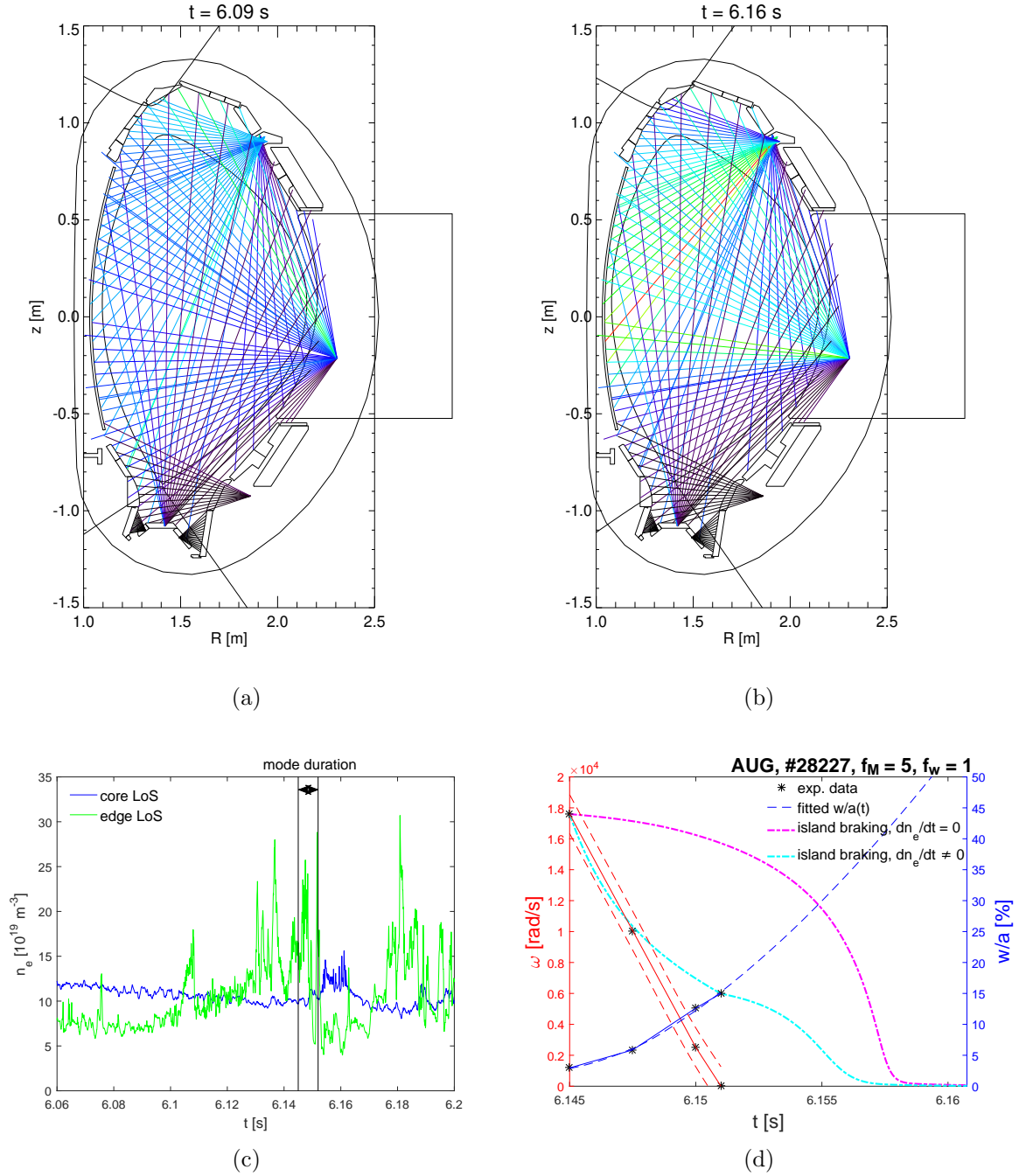
Figure 13: Illustration of an attempt to reconstruct the braking curve in NBI-heated discharge #28227. (a) and (b) display AXUV diode bolometry signals, colour-coded according to relative emissivity (dark blue = low emissivity, light green = medium, red = high). In (a), at $t = 6.09$ s, a cold region has developed and is visible in the channels viewing the vessel HFS bottom. (b) At $t = 6.16$ s the cold region is recognizable near the inner midplane. (c) Line-integrated electron density measurements from the CO_2 interferometer. The core LOS is nearly unaffected by the cold and dense region, while in the edge channel its influence can be clearly noticed between about 6.1 and 6.2 s. In particular, during the presence of the mode, the density reaches $\approx 2.5 \times 10^{19}$ m^{-3}. (d) Comparison of braking curves obtained by integrating the mode equation either with a modelled local particle source (equation (27), cyan dotted) or without (magenta dash-dotted).

island width for locking. The model for mode deceleration incorporated the braking force due to electromagnetic interaction between the mode and the conducting vessel wall, as well as the restoring viscous force and its degradation due to growth of the mode.

The mode braking model showed its merit in describing deceleration of large modes locking over temporal intervals comparable to the momentum confinement time, in case the mode deceleration phase was initiated in a quasi-stationary rotating plasma column. Under such conditions the model could predict the duration of the braking phase. On the other hand, the theoretical critical mode width for locking, set at the dynamic point of the locking bifurcation, could not be reliably compared with the experiment due to limitations in the locking bifurcation definition.

For a substantial fraction of discharges, often those occurring in high-density plasmas, the calculated wall torque was not sufficient to reproduce the locking dynamics and the braking of the initially rotating modes could not be explained on the basis of the physical mechanisms contained in the model. To increase the predictive capability of the model for plasmas experiencing a transient increase of the plasma density in the vicinity of the mode location, it was proposed to add a local particle source in the mode equation of motion.

Future experimental tokamak devices like ITER will operate close to the limits of the non-disruptive plasma parameter space, i.e. under conditions favourable for seeding of (initially rotating) MHD modes. The present case study for AUG showed that disruption avoidance schemes that aim to tailor the features of rotating modes will need to consider all boundaries of the non-disruptive operational space. It remains to be seen whether this observation is also valid for other devices.

Acknowledgements

A   Appendix

A.1   Perturbation field components in the vicinity of a resistive wall (cylindrical plasma)

Features of the magnetic field $\tilde{\boldsymbol{B}}$ of a helical mode structure can be derived by defining an associated scalar flux function of the form $\tilde{\psi}(r, \theta, \phi) = \tilde{\psi}_r(r)e^{i(m\theta - n\phi - \omega t)}$. Radial and poloidal components of $\tilde{\boldsymbol{B}}$ are retrieved using [13, 18, 26]

$$\tilde{B}_r = -\frac{1}{r}\frac{\partial \tilde{\psi}_r}{\partial \theta} = -\frac{im}{r}\tilde{\psi}_r, \tag{28}$$

$$\tilde{B}_\theta = \frac{\partial \tilde{\psi}}{\partial r}. \tag{29}$$

A mode located at $r = r_{\mathrm{s}}$ is a source of surface current $\tilde{J}_{\mathrm{s}}(r, \theta, \phi) = J_{\mathrm{s}}^{\dagger}\delta(r - r_{\mathrm{s}})e^{i(m\theta - n\phi - \omega t)}$ and induces in the wall a current $\tilde{J}_{\mathrm{w}}(r, \theta, \phi) = J_{w}^{\dagger}\delta(r - r_{\mathrm{w}})e^{i(m\theta - n\phi - \omega t)}$, where $J_{s}^{\dagger}$ and $J_{w}^{\dagger}$ are constants. In the thin-wall approximation (thickness b), this current is assumed uniform over the wall layer: $\tilde{J}_{\mathrm{w}} = j_{\mathrm{w}}b$. Currents in the resistive wall decay on a time scale τ_{w} and induce an electric field $E_{\mathrm{w},\phi}$ along the helical coordinate. A solution of the flux function

in the radial domains $r < r_{\rm s}$ (I), $r_{\rm w} < r < r_{\rm s}$ (II) and $r > r_{\rm w}$ (III) is obtained by solving Ampère's equation, with appropriate boundary conditions:

$$\tilde{\psi}_{\rm I} = \frac{\psi^\dagger}{m} \left[1 - \frac{\omega\tau_{\rm w}}{im + \omega\tau_{\rm w}} \left(\frac{r_{\rm s}}{r_{\rm w}} \right)^{2m} \right] \left(\frac{r}{r_{\rm s}} \right)^m e^{i(m\theta - n\phi - \omega t)}, \tag{30}$$

$$\tilde{\psi}_{\rm II} = \frac{\psi^\dagger}{m} \left[\left(\frac{r_{\rm s}}{r} \right)^m - \frac{\omega\tau_{\rm w}}{im + \omega\tau_{\rm w}} \left(\frac{r_{\rm s}}{r_{\rm w}} \right)^{2m} \left(\frac{r}{r_{\rm s}} \right)^m \right] e^{i(m\theta - n\phi - \omega t)}, \tag{31}$$

$$\tilde{\psi}_{\rm III} = \frac{\psi^\dagger}{m} \left[1 - \frac{\omega\tau_{\rm w}}{im + \omega\tau_{\rm w}} \right] \left(\frac{r_{\rm s}}{r} \right)^m e^{i(m\theta - n\phi - \omega t)}. \tag{32}$$

where $\psi^\dagger = \mu_0 J_{\rm s}^\dagger r_{\rm s}/2$. Invoking (28) and (29), relations between the radial and poloidal components of the mode magnetic field can be established:

$$\tilde{B}_{r,{\rm I}} = -i\tilde{B}_{\theta,{\rm I}}, \tag{33}$$

$$\tilde{B}_{r,{\rm II}}/\tilde{B}_{\theta,{\rm II}} = i \frac{\frac{im + \omega\tau_{\rm w}}{\omega\tau_{\rm w}} r_{\rm w}^{2m} - r^{2m}}{\frac{im + \omega\tau_{\rm w}}{\omega\tau_{\rm w}} r_{\rm w}^{2m} + r^{2m}}, \tag{34}$$

$$\tilde{B}_{r,{\rm III}} = i\tilde{B}_{\theta,{\rm III}}. \tag{35}$$

The above relations were used to retrieve the radial component $\tilde{B}_r(r_{\rm s})$ of the mode's magnetic field at the rational surface, from $\tilde{B}_\theta(r_{\rm c})$ measured at the coil position $r_{\rm c}$. This results in

$$\frac{|\tilde{B}_r(r_{\rm s})|}{|\tilde{B}_\theta(r_{\rm c})|} = \left(\frac{r_{\rm c}}{r_{\rm s}} \right)^{m+1} \frac{\left\{ m^2 r_{\rm w}^{4m} \omega^2 \tau_{\rm w}^2 (r_{\rm s}^{2m} + r_{\rm c}^{2m})^2 + [m^2 r_{\rm w}^{4m} + \omega^2 \tau_{\rm w}^2 (r_{\rm w}^{2m} - r_{\rm s}^{2m})(r_{\rm w}^{2m} + r_{\rm c}^{2m})]^2 \right\}^{1/2}}{\omega^2 \tau_{\rm w}^2 (r_{\rm w}^{2m} + r_{\rm c}^{2m})^2 + m^2 r_{\rm w}^{4m}}. \tag{36}$$

The ratio of the perturbation field inside ('in') and outside ('out') the conducting structure can be obtained using (31), (32) and (29). This yields

$$\frac{|\tilde{B}_{\theta,{\rm out}}|}{|\tilde{B}_{\theta,{\rm in}}|} = \left[\frac{m^2 + \omega^2 \tau_{\rm w}^2}{m^2} \left(\frac{r_{\rm c,out}}{r_{\rm c,in}} \right)^{m+1} + \frac{\omega^2 \tau_{\rm w}^2}{m^2} \frac{(r_{\rm c,in})^{m-1}(r_{\rm c,out})^{m+1}}{r_{\rm w}^{2m}} \right]^{-1}. \tag{37}$$

Furthermore, from the expressions of the flux function in (31) and (32), the phase difference $\Delta\tilde{\theta}$ across the wall can be derived. This depends on the wall properties and is related to the force through which the mode loses its momentum to the wall. The poloidal angle θ represents the angle by which the sensors are displaced along the poloidal coordinate. Similar to (37), an expression for the phase shift can be established, depending on ω and $\tau_{\rm w}$.

A.2 Perturbation field components in the vacuum approximation corrected for the effect of toroidicity

Bending the plasma column in an axisymmetric configuration implies correction of the flux function solutions (Eqs. (30)–(32), here considered in the vacuum limit) for the effect of toroidicity, both along the radial and poloidal coordinates. This is because modes of the same toroidal mode number n, but different poloidal mode number m, become coupled. In [17], it is shown that the amplitude modulation $\tilde{A}(\theta, \phi)$ in an axisymmetric tokamak of circular cross-section is the following:

$$\tilde{A}(\theta, \phi) = \tilde{A}\cos(m\theta - n\phi) + \frac{\tilde{A}_1}{2}\left\{ \cos[(m-1)\theta - n\phi - \varphi_1] + \cos[(m+1)\theta - n\phi + \varphi_1] \right\}. \tag{38}$$

In this expression, $\tilde{A}$ is the amplitude of the perturbation at a given point along the radial coordinate. The first term on the right-hand side represents the phase of the flux function related to the cylindrical geometry. The second term appears after modulation of the amplitude

when passing to the case of generalized geometry, retrieved upon Fourier series expansion of the amplitude in the poloidal θ coordinate. The effect of toroidicity is pronounced for $j = 1$ and the $\Delta m = \pm 1$ sidebands justify the existence of the toroidally coupled modes. The same conclusion can be obtained by accounting for the Merezhkin correction, expressing the phase in terms of a Bessel function of the first kind $J(\pm 1, m\lambda)$ [18]. This approach allows estimating the amplitude $\tilde{A}_1$ (under the condition $m\lambda \ll 1$),

$$\tilde{A}_1 = \tilde{A} m\lambda \approx \tilde{A}\frac{r}{R}, \tag{39}$$

where $\lambda \approx \beta_{\mathrm{p}} + l_{\mathrm{i}}/2 + 1$. The effect of toroidicity on the radially-dependent part of the flux function solution can be examined by combining (31) (vacuum limit) and (39), yielding exact solutions of the sideband flux functions for $r > r_{\mathrm{s},m+1}$:

$$\tilde{\psi}(r) = \frac{\psi^{\dagger}}{m+1}\left(\frac{r_{\mathrm{s},m}}{r}\right)^{m+1}\cos[(m+1)\theta]J(+1, m\lambda)\left(\frac{R_0}{r\cos\theta + R_0}\right), \tag{40}$$

$$\tilde{\psi}(r) = \frac{\psi^{\dagger}}{m-1}\left(\frac{r_{\mathrm{s},m}}{r}\right)^{m-1}\cos[(m-1)\theta]J(-1, m\lambda)\left(\frac{R_0}{r\cos\theta + R_0}\right). \tag{41}$$

The last term in (40) and (41) results from the $1/R$-dependence of the helical field in toroidal geometry, which for large aspect ratio expands to $1/(r\cos\theta + R_0)$. The R_0 term in the nominator is added for normalization purposes. The perturbation field components in toroidal geometry are the following:

$$\tilde{B}_{r,\mathrm{tor}} = -\frac{1}{2\pi R}\frac{1}{r}\frac{\partial\tilde{\psi}}{\partial\theta}, \tag{42}$$

$$\tilde{B}_{\theta,\mathrm{tor}} = \frac{1}{2\pi R}\frac{\partial\tilde{\psi}}{\partial R}. \tag{43}$$

For given λ, the full solution including the effect of toroidicity is obtained by adding the sidebands to the cylindrical case. In Fig. 14, the radial decay of $\tilde{B}_{\theta,\mathrm{tor}}$ for the case of the midplane low-field side ($\theta = 0$, $R_0 = 1.65$, $r_{\mathrm{s}} = 0.4$ m) is plotted for progressively increasing λ, $m = 2$. The curves were fitted with an analytical function of the form $\alpha r^{m_{\mathrm{eff}}}$ in the range $r = 0.5$ m to 1 m (dashed lines). The m number was varied from 2 to 4 and the resulting scaling relations can be used in the expression for the mode poloidal field component, replacing m with its effective equivalent m_{eff}, accounting for the effect of toroidicity. Taking $\lambda = 0.4$ and adopting medians of β_{p} and l_{i} from Tab. 3, we obtain for the high-field side (HFS) and low-field side (LFS):

$$m_{\mathrm{eff},\theta,\mathrm{HFS}} = 2.57\,m - 1.30, \tag{44}$$

$$m_{\mathrm{eff},\theta,\mathrm{LFS}} = 0.81\,m + 0.03, \tag{45}$$

respectively. In case of the vacuum solution, the radial component of the perturbation field vanished at the LFS and HFS midplane. Given the symmetry of the problem, $\tilde{B}_{r,\mathrm{tor}}(\theta = \pi/2) = \tilde{B}_{r,\mathrm{tor}}(\theta = 3\pi/2)$, the resulting scaling relation for the effective mode numbers is:

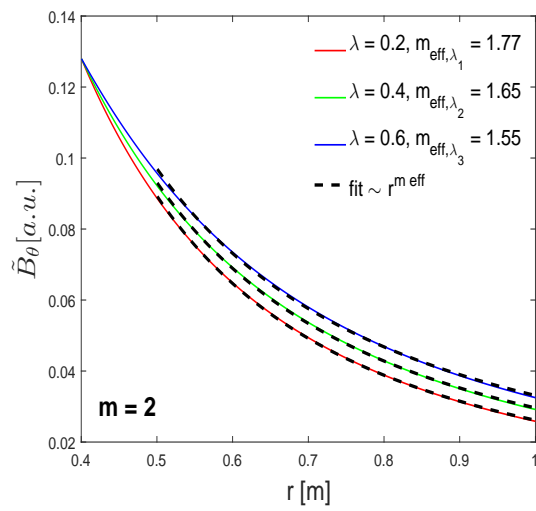$$m_{\mathrm{eff},r} = 0.98\,m + 0.86. \tag{46}$$

Figure 14: Radial decay of the poloidal component of the perturbation field, showing the effect of toroidicity for various λ.

References

[1] LEHNEN, M. 2015 *Journal of Nucl. Materials* **463** 39-48

[2] DE VRIES, P.C. et al. 2011 *Nucl. Fusion* **51** 053018

[3] DE VRIES, P.C. et al. 2016 *Nucl. Fusion* **56** 026007

[4] SOZZI, C. et al. 2018 Early Identification of Disruption Paths for Prevention and Avoidance *Poster presented at 27th IAEA Fusion Energy Conference (Ahmedabad, India)* http://hdl.handle.net/21.11116/0000-0002-6F70-4

[5] OKABAYASHI, M. et al. 2013 Avoidance of Neoclassical Tearing Mode Locking and Disruption by Feedback-Induced Accelerating Electro-Magnetic Torque *Proc. of the 40th EPS Conf. on Plasma Physics (Espoo, Finland)* http://ocs.ciemat.es/EPS2013PAP/pdf/P2.152.pdf

[6] MORRIS, A.W. et al. 1990 *Phys. Review Letters* **64** 1254

[7] HAM, J. et al. 2011 *Plasma Phys. Contr. Fusion* **53** 085003

[8] SNIPES, J. et al. 1990 *Nucl. Fusion* **30** 205

[9] CHANG, Z. and CALLEN, J.D. 1990 *Nucl. Fusion* **30** 219

[10] HOLMES, J.A. et al. 1979 *Nucl. Fusion* **19** 1333

[11] ESPOSITO, B. et al. 2011 *Nucl. Fusion* **53** 124035

[12] GRANUCCI, G. et al. 2015 Stable Operation at Disruptive Limits by Means of EC at ASDEX Upgrade *Proc. of the 42nd EPS Conf. on Plasma Physics (Vienna, Austria)* https://pdfs.semanticscholar.org/b5b5/23e9a2276659634036044619606bd42302a5.pdf

[13] NAVE, M.F.F. and WESSON, J.A. 1990 *Nucl. Fusion* **30** 2575

[14] LA HAYE, R.J. et al. 2006 *Nucl. Fusion* **46** 451

[15] GATES, D.A. and HENDER, T.C. 1996 *Nucl. Fusion* **36** 273

[16] BRAND, H. et al. 2012 *Plasma Phys. Contr. Fusion* **54** 094003

[17] IGOCHINE, V. et al. 2015 *Active control of magnetohydrodynamic instabilities in hot plasmas*, Springer

[18] ZOHM, H., 2014 *Magnetohydrodynamic stability of tokamaks*,Germany: Wiley-VCH

[19] IGOCHINE, V. and CALLEN, J.D. 2017 *Nucl. Fusion* **57** 116027

[20] STIX, T.H. 1973 *Physics of Fluids* **16** 1260

[21] KALLENBACH, A. et al. *Plasma Phys. Contr. Fusion* **33** (1991) 595

[22] SNIPES, J. et al. 1988 *Nucl. Fusion* **28** 1085

[23] FITZPATRICK, R. 1993 *Nucl. Fusion* **33** 1049

[24] DE VRIES, P.C. et al. 1996 *Plasma Phys. Contr. Fusion* **38** 467

[25] CHAPMAN, B.E. et al. 2004 *Physics of Plasmas* **11** 5

[26] WESSON, J., 2011 *Tokamaks*, USA: Oxford University Press, Inc.,

[27] PAUTASSO, G. et al. 2014 Disruption causes in ASDEX Upgrade *Proc. of the 40th EPS Conf. on Plasma Physics (Berlin, Germany)* `http://ocs.ciemat.es/EPS2014PAP/pdf/P2.015.pdf`

[28] GREENWALD, M. et al. 1988 *Nucl. Fusion* **28** 2199

[29] BERNERT, M. et al. 2014 *Plasma Phys. Contr. Fusion* **57** 014038

[30] LIPSCHULTZ, B. et al. 1984 *Nucl. Fusion* **24** 977

[31] CHENG, C.Z. et al. 1987 *Plasma Phys. Contr. Fusion* **29** 351

[32] MC CARTHY, P.J. et al. 1999 *The CLISTE interpretive equilibrium code*, Germany, IPP Garching, IPP 5/85

[33] TRANSP REFERENCES 1998 https://w3.pppl.gov/transp/refs

[34] LAURENT, L. 1994 *International workshop on tokamak concept improvement (Varenna, Italy)* INIS Volume **28** 28016718

[35] LOGAN, P.C. et al. 2010 *Plasma Phys. Contr. Fusion* **52** 045013

[36] MARASCHEK, M. et al. 2013 Measurement and impact of the n=1 intrinsic error field at ASDEX Upgrade *Proc. of the 40th EPS Conf. on Plasma Physics (Espoo, Finland)* `http://ocs.ciemat.es/EPS2013PAP/pdf/P4.127.pdf`

[37] ZOHM, H. et al. 1990 *Europhys. Lett.* **11** 745